Euro. Jnl of Applied Mathematics (2007), *vol.* 18, *pp.* 631–657. © 2007 Cambridge University Press
doi:10.1017/S095679250700719X Printed in the United Kingdom

Stress- and diffusion-induced interface motion: Modelling and numerical simulations

HARALD GARCKE[a], ROBERT NÜRNBERG[b] and VANESSA STYLES[c]

[a]*Naturwissenschaftliche Fakultät I - Mathematik, Universität Regensburg, 93040 Regensburg, Germany*
[b]*Department of Mathematics, Imperial College London, London, SW7 2AZ, UK*
[c]*Department of Mathematics, University of Sussex, Brighton, BN1 9RF, UK*

(*Received 24 April 2007; revised 7 September 2007*)

We propose a phase field model for stress and diffusion-induced interface motion. This model, in particular, can be used to describe diffusion-induced grain boundary motion and generalizes a model of Cahn, Fife and Penrose as it more accurately incorporates stress effects. In this paper we will demonstrate that the model can also be used to describe other stress-driven interface motion. As an example, interface motion resulting from interactions of interfaces with dislocations is studied.

1 Introduction

Interface migration, such as grain boundary motion in polycrystalline materials, can have different driving forces. A curved interface (or, more precisely, an interface with a non-zero mean curvature) will tend to move in order to reduce its interfacial energy. In fact, as was first discussed by Mullins [29], the interface will locally move to the centre of curvature. When an interface is subjected to internal or external mechanical stresses, a difference in stress across the interface leads to a driving force which is given by the normal component of Eshelby's [12] 'energy-momentum' tensor. For example, internal stresses can be caused when a polycrystalline film of a metal is placed in a vapour containing another metal. Then atoms diffuse into the film through grain boundaries and elastic stresses can result due to a lattice misfit (see, e.g. Handwerker [24] and Sutton and Balluffi [33]).

In this paper, we introduce a phase field model for interface motion, taking into account driving forces due to interfacial and elastic energies, and we allow for diffusion of atoms in the interface. We in particular generalize models that have been studied earlier (we refer to [1, 4, 6, 18, 19, 22, 26, 28, 30]). Phase field models for stress-driven interface motion have been used, for example to describe spinodal decomposition under stress, martensitic transformations, evolution of thin films and crystal growth under stress (we refer to the recent reviews [7, 20] and the references therein). A phase field model for diffusion-induced grain boundary motion (DIGM) has been introduced by Cahn *et al.* [6]. In this model, an elastic driving force for DIGM was included through an approximation of the elastic energy density. The main goal of this work is to derive a phase field model incorporating the elastic effects more accurately. Another issue in the modelling of DIGM is to come up with a model that is able to describe bidirectional grain boundary motion. There are

https://doi.org/10.1017/S095679250700719X Published online by Cambridge University Press

models for bidirectional motion in the literature (see e.g. [11, 15, 22]) but they also do not include elastic effects accurately. We will demonstrate in this paper that elastic effects in fact can lead to bidirectional motion during the evolution of grain boundaries.

The model introduced in this paper couples an Allen–Cahn equation to an elasticity system and a diffusion equation. We will relate this phase field model to a sharp interface model by matched asymptotic expansions. The main part of the paper will be concerned with the numerical approximation of the phase field model to demonstrate that several phenomena can be described with the help of our model. We also construct new explicit one-dimensional and radial solutions for stress-driven interface motion. In the radial situation, explicit solutions for a situation in which mean curvature flow is coupled to elasticity are presented. These explicit solutions help to understand the influence of the different parameters in the system, and they are also used to compare numerical solutions from phase field computations with exact solutions of the sharp interface problem. Furthermore, it is possible to identify a critical size for a nucleus in order that it can grow in situations with driving forces due to interfacial and elastic energies.

2 The phase field model

2.1 Derivation

We will consider a diffuse interface model with a phase field φ which attains the values ± 1 in the bulk and the region $-1 < \varphi < 1$ is the diffuse interface that represents the grain boundary. As further field variables, we use the concentration c and the displacement vector $\mathbf{u} \in \mathbb{R}^d$ (d being the spatial dimension). All functions depend on a spatial variable $\mathbf{x}$ and the time variable t. The theory is based on linear elasticity so that the strain tensor is given by

$$\mathscr{E}(\nabla \mathbf{u}) := \frac{1}{2}(\nabla \mathbf{u} + (\nabla \mathbf{u})^T).$$

We study a phase field model with the following Ginzburg–Landau free energy

$$\mathscr{F}(\varphi, c, \mathbf{u}) = \int_\Omega \left(\frac{1}{2\varepsilon} c^2 + \frac{\varepsilon}{2} |\nabla \varphi|^2 + \frac{1}{\varepsilon} \Psi(\varphi) + W(\mathbf{x}, \varphi, c, \mathscr{E}(\nabla \mathbf{u})) + p(\varphi, c) \right), \tag{2.1}$$

where $\Omega \subset \mathbb{R}^d$. The first term in the free energy takes into account the chemical energy, the second and third terms represent interfacial energy (cf. [1, 10]) and the fourth term,

$$W(\mathbf{x}, \varphi, c, \mathscr{E}) = \frac{1}{2}(\mathscr{E} - \bar{\mathscr{E}}(\mathbf{x}, \varphi, c)) : \mathscr{C}(\mathbf{x}, \varphi, c)(\mathscr{E} - \bar{\mathscr{E}}(\mathbf{x}, \varphi, c)), \tag{2.2}$$

models the elastic energy, where the product $\mathscr{A} : \mathscr{B}$ of two $d \times d$ matrices $\mathscr{A}, \mathscr{B}$ is defined to be $\sum_{i,j=1}^d \mathscr{A}_{ij} \mathscr{B}_{ij}$. The last term in (2.1) takes interactions between φ and c into account (see also [6]). Since we want to concentrate on the interactions due to elastic contributions, we will in this paper often set the term $p(\varphi, c)$ to be zero.

By $\mathscr{C}(\mathbf{x}, \varphi, c)$ we denote the possibly anisotropic elasticity tensor that we assume to be positive definite and complying with the usual symmetry conditions of linear elasticity. The term $\bar{\mathscr{E}}(\mathbf{x}, \varphi, c)$ is the stress-free strain. This is the energetically favourable state for the strain tensor. In the following we will assume analogously to Vegard's law that the

https://doi.org/10.1017/S095679250700719X Published online by Cambridge University Press

stress-free strain varies affine linearly with φ and c. We therefore set

$$\bar{\mathscr{E}}(\mathbf{x},\varphi,c)=\bar{\mathscr{E}}_1(\mathbf{x})\varphi+\bar{\mathscr{E}}_2(\mathbf{x})c+\bar{\mathscr{E}}_3(\mathbf{x}).$$

Often we take an elasticity tensor that only depends on φ, in particular we consider the following structure

$$\mathscr{C}(\varphi)=\mathscr{C}^-+\frac{1}{2}(1+\varphi)(\mathscr{C}^+-\mathscr{C}^-) \tag{2.3}$$

with constant tensors $\mathscr{C}^-$, $\mathscr{C}^+$, which are the elasticity tensors of the two grains, which we denote by $-$ and $+$ such that $\mathscr{C}=\mathscr{C}^\pm$ when $\varphi=\pm 1$. For the constant tensors $\mathscr{C}^-$ and $\mathscr{C}^+$, we assume positive definiteness and the usual symmetry conditions of linear elasticity:

$$\mathscr{C}^\pm_{ijmn}=\mathscr{C}^\pm_{ijnm}=\mathscr{C}^\pm_{jimn}=\mathscr{C}^\pm_{mnij}. \tag{2.4}$$

In the two-dimensional case we uniquely define a tensor $\mathscr{C}$ that satisfies the symmetry conditions (2.4) by its 6 degrees of freedom

$$\mathscr{C}=(\mathscr{C}_{1111},\mathscr{C}_{1112},\mathscr{C}_{1122},\mathscr{C}_{1212},\mathscr{C}_{1222},\mathscr{C}_{2222}). \tag{2.5}$$

Of course, generalizations including elasticity tensors depending on c can also be treated. For Ψ we take the classical obstacle potential (see [5]) that is defined to be

$$\Psi(\varphi)=\begin{cases}\frac{1}{2}(1-\varphi^2) & \text{for } -1\leqslant\varphi\leqslant 1,\\ \infty & \text{otherwise.}\end{cases} \tag{2.6}$$

In the above, to simplify the presentation, we have set most of the material constants to be one and we refer to subsection 2.2 for a non-dimensionalization in the sharp interface situation. Also we use a subscript φ, c or $\mathbf{u}$ to denote differentiation with respect to φ, c or $\mathbf{u}$, for example $W_{,\varphi}=\frac{\partial W}{\partial\varphi}$.

Equations of motion for φ are derived by considering the L^2-gradient flow of (2.1) with respect to φ, giving an Allen-Cahn–type equation:

$$\varepsilon\frac{\partial\varphi}{\partial t}=-\frac{\delta\mathscr{F}}{\delta\varphi}(\varphi,c,\mathbf{u})=\varepsilon\Delta\varphi-\frac{1}{\varepsilon}\Psi_{,\varphi}(\varphi)-W_{,\varphi}(\cdot,\varphi,c,\mathscr{E}(\nabla\mathbf{u}))-p_{,\varphi}(\varphi,c), \tag{2.7}$$

together with the natural boundary condition

$$\nabla\varphi\cdot\nu_{\partial\Omega}=0 \quad \text{on } \partial\Omega.$$

Here $\frac{\delta\mathscr{F}}{\delta\varphi}$ denotes the functional derivative with respect to φ and $\nu_{\partial\Omega}$ is the outer unit normal to $\partial\Omega$. We remark that (2.7) needs to be interpreted as a variational inequality if Ψ has the double obstacle form (2.6) (see [10]). Since the concentration c obeys a conservation law, we couple (2.7) with, as in [6], a kinetic equation with conserving dynamics for c (which has to be interpreted in an appropriate weak formulation; see [9])

$$\frac{\partial c}{\partial t}=\nabla\cdot\left(D(\varphi)\nabla\frac{\delta\mathscr{F}}{\delta c}(\varphi,c,\mathbf{u})\right) \quad \text{in } \Omega,$$

https://doi.org/10.1017/S095679250700719X Published online by Cambridge University Press

which is equivalent to

$$\varepsilon \frac{\partial c}{\partial t} = \nabla \cdot (D(\varphi)\nabla v) \quad \text{in } \Omega, \tag{2.8}$$

with the scaled chemical potential

$$v = c + \varepsilon\, W_{,c}(\cdot, \varphi, c, \mathscr{E}(\nabla \mathbf{u})) + \varepsilon p_{,c}(\varphi, c). \tag{2.9}$$

Equation (2.8) is supplemented with the Newton flux boundary condition

$$D(\varphi)\frac{\partial v}{\partial \nu_{\partial\Omega}} = \alpha D(\varphi)(1 - c) \quad \text{on } \partial\Omega,$$

where α is a large positive number. The diffusivity

$$D(\varphi) = \frac{\pi}{2} D_c(1 - \varphi^2), \qquad D_c \in \mathbb{R}_{>0},$$

is chosen such that diffusion is restricted to the interfacial regions, that is we assume that we can neglect diffusion in the bulk.

For DIGM we consider the following two-dimensional experimental set-ups.

- *The thin film set-up*: The domain $\Omega \subset \mathbb{R}^2$, on which we work, corresponds to a horizontal cross section through the polycrystalline film. In this set-up the concentration of solute is assumed to be constant through the film and hence we do not need to take the diffusion equation into account. For this set-up we consider cases in which an interface moves due to inner stresses resulting, for example from dislocations as well as from applied outer stresses.
- *The thick film set-up*: The domain $\Omega \subset \mathbb{R}^2$ corresponds to a vertical cross section through the polycrystalline film. In this set-up we have to take diffusion in grain boundaries into account such that the concentration satisfies a diffusion equation on the grain boundary.

If the geometry is such that the specimen under consideration is thin, it can be assumed that the diffusion of solute atoms is rapid so that (2.8) can be replaced by (see also [11])

$$c(\mathbf{x}, t) = \begin{cases} 1 & \forall\ (\mathbf{x}, t) \text{ such that } |\varphi(\mathbf{x}, \bar{t})| < 1 \text{ for a } \bar{t} \in [0, t], \\ 0 & \text{otherwise.} \end{cases} \tag{2.10}$$

Since the relaxation into mechanical equilibrium occurs on a time scale that is fast compared to the time scale at which diffusion takes place, we assume quasi-static equilibrium for the deformation. Hence, $\frac{\delta \mathscr{F}}{\delta \mathbf{u}} = 0$, which implies

$$\nabla \cdot \mathscr{S} = \nabla \cdot W_{,\mathscr{E}} = \nabla \cdot [\mathscr{C}(\mathbf{x}, \varphi, c)(\mathscr{E}(\nabla \mathbf{u}) - \bar{\mathscr{E}}(\mathbf{x}, \varphi, c))] = 0, \tag{2.11}$$

where $\mathscr{S} = \mathscr{C}(\mathbf{x}, \varphi, c)(\mathscr{E}(\nabla \mathbf{u}) - \bar{\mathscr{E}}(\mathbf{x}, \varphi, c))$ is the stress tensor. At the boundary we impose outer stresses of the form

$$\mathscr{S} \nu_{\partial\Omega} = \mathscr{S}^* \nu_{\partial\Omega}$$

with a constant symmetric tensor $\mathscr{S}^*$.

https://doi.org/10.1017/S095679250700719X Published online by Cambridge University Press

Remark In this paper we replace (2.9) by $v = c$. It was demonstrated in [9, 13] that this does not change the limiting sharp interface problem.

2.2 Weak formulation

By $(\cdot,\cdot)$ we will denote in the following the standard L^2 inner product over Ω. To write the elastic terms more conveniently, we introduce for a given tensor $\mathscr{C}$ the following scalar product of two matrix-valued functions $\mathscr{A}$ and $\mathscr{B}$:

$$\langle \mathscr{A}, \mathscr{B} \rangle_{\mathscr{C}} := (\mathscr{A}, \mathscr{C}\mathscr{B}) = \int_\Omega \mathscr{A} : \mathscr{C}\mathscr{B}.$$

We note that since W is given by (2.2) we have that for suitable test functions η

$$\begin{aligned}(W_{,\varphi}, \eta) &= \int_\Omega W_{,\varphi}\,\eta = \int_\Omega \left(\frac{1}{2}(\mathscr{E} - \bar{\mathscr{E}}) : \mathscr{C}_{,\varphi}(\mathscr{E} - \bar{\mathscr{E}}) - \bar{\mathscr{E}}_{,\varphi} : \mathscr{C}(\mathscr{E} - \bar{\mathscr{E}}) \right) \eta \\ &= \frac{1}{2}\langle \mathscr{E} - \bar{\mathscr{E}}, \eta(\mathscr{E} - \bar{\mathscr{E}}) \rangle_{\mathscr{C}_{,\varphi}} - \langle \mathscr{E} - \bar{\mathscr{E}}, \eta\ \bar{\mathscr{E}}_{,\varphi} \rangle_{\mathscr{C}}.\end{aligned}$$

The weak form of (2.7), taking into account the obstacle potential Ψ, can be written as (see also [10])

$$\begin{aligned}\varepsilon \left(\frac{\partial \varphi}{\partial t}, \eta - \varphi \right) \geqslant\ & -\varepsilon (\nabla \varphi, \nabla(\eta - \varphi)) + \frac{1}{\varepsilon}(\varphi, \eta - \varphi) - (p_{,\varphi}(\varphi, c), \eta - \varphi) \\ & - \frac{1}{2}\langle \mathscr{E}(\nabla \mathbf{u}) - \bar{\mathscr{E}}(\mathbf{x}, \varphi, c), (\eta - \varphi)(\mathscr{E}(\nabla \mathbf{u}) - \bar{\mathscr{E}}(\mathbf{x}, \varphi, c)) \rangle_{\mathscr{C}_{,\varphi}(\varphi)} \\ & + \langle \mathscr{E}(\nabla \mathbf{u}) - \bar{\mathscr{E}}(\mathbf{x}, \varphi, c), (\eta - \varphi)\bar{\mathscr{E}}_{,\varphi}(\mathbf{x}, \varphi, c) \rangle_{\mathscr{C}(\varphi)} \quad \forall\ \eta \in K, \end{aligned} \tag{2.12}$$

where

$$K = \{\eta \in H^1(\Omega) : |\eta| \leqslant 1 \text{ in } \Omega\}$$

is a subset of the Sobolev space $H^1(\Omega)$. Testing (2.8) and (2.11) with test functions in $H^1(\Omega)$ yields (where $\langle \cdot, \cdot \rangle$ is the duality pairing in $H^1(\Omega)$), on recalling that $v = c$, that

$$\varepsilon \left\langle \frac{\partial c}{\partial t}, \xi \right\rangle + \int_\Omega D(\varphi) \nabla c \cdot \nabla \xi = \alpha \int_{\partial\Omega} D(\varphi)(1 - c)\xi \quad \forall\ \xi \in H^1(\Omega) \tag{2.13}$$

and

$$\langle \mathscr{E}(\nabla \mathbf{u}) - \bar{\mathscr{E}}(\mathbf{x}, \varphi, c), \mathscr{E}(\nabla \boldsymbol{\xi}) \rangle_{\mathscr{C}} = \int_{\partial\Omega} \boldsymbol{\xi} \cdot \mathscr{S}^* \nu_{\partial\Omega} \quad \forall\ \boldsymbol{\xi} \in (H^1(\Omega))^d, \tag{2.14}$$

while a time relaxation of (2.10) with relaxation time Λ yields

$$\varepsilon \left(\frac{\partial c}{\partial t}, \chi - c \right) \geqslant \Lambda(1 - \varphi^2, \chi - c) \quad \forall\ \chi \in \tilde{K}, \tag{2.15}$$

where

$$\tilde{K} = \{\eta \in L^2(\Omega) : 0 \leqslant \eta \leqslant 1\}.$$

https://doi.org/10.1017/S095679250700719X Published online by Cambridge University Press

As initial data we set

$$\varphi(\mathbf{x},0)=\varphi_0(\mathbf{x}),\quad c(\mathbf{x},0)=c_0(\mathbf{x})\qquad \forall\ \mathbf{x}\in\Omega. \tag{2.16}$$

Often we will take $c_0=0$, which implies that initially no solute is present.

3 The sharp interface model

3.1 Formulation of the model

In this section we state a sharp interface model for stress and diffusion-induced interface motion in the presence of surface effects. In the Appendix we will relate this sharp interface model and the phase field model of Section 2 by formal asymptotics. In a sharp interface model, two phases that occupy domains Ω^- and Ω^+ are separated by a sharp interface Γ. The fields of interest $\mathbf{u},\mathscr{E},\mathscr{S},c$ are given in Ω^- and Ω^+ and some of these quantities may jump across the interface Γ.

One governing equation for Γ separating the bulk phases Ω^- and Ω^+ is given by the kinetic law

$$V=\kappa+\frac{2}{\pi}\nu\cdot[W\,\mathrm{Id}-(\nabla\mathbf{u})^T\mathscr{S}]^+_-\nu, \tag{3.1}$$

where Id is the identity, V and κ denote the normal velocity and the mean curvature of the interface Γ with respect to the normal ν pointing from Ω^- to Ω^+ and $[f]^+_-$ denotes the jump across the interface such that for all $\mathbf{x}\in\Gamma$

$$[f]^+_-=\lim_{\delta\to 0^+}\{f(\mathbf{x}+\delta\nu)-f(\mathbf{x}-\delta\nu)\}.$$

Furthermore, we replace (2.8) and (2.9) in the sharp interface model by the following equation for the concentration c

$$-V\,[c]^+_-=D_c\,\Delta_\Gamma c\quad\text{on}\quad\Gamma, \tag{3.2}$$

where Δ_Γ is the surface Laplacian on Γ. In the case $d=2$ we obtain $\Delta_\Gamma c=c_{,ss}$ where s denotes the arclength of Γ. The condition (2.10) has to be replaced by

$$c(\mathbf{x},t)=\begin{cases}1 & \forall\ (\mathbf{x},t)\text{ such that }\mathbf{x}\in\Gamma_{\bar t}\text{ for a }\bar t\in[0,t],\\ 0 & \text{otherwise,}\end{cases} \tag{3.3}$$

where Γ_t is the interface at time t.

At points B, where the interface Γ meets the outer boundary $\partial\Omega$, it must do so orthogonally (see [31]) and the concentration c has to satisfy

$$D_c\nabla_\Gamma c\cdot\nu_{\partial\Omega}=\alpha(1-c)\qquad\text{at } B. \tag{3.4}$$

Here ∇_Γ is the surface gradient on Γ, which for $d=2$ reduces to $c_{,s}\tau$, where τ points in the direction of increasing s. Denoting by $\mathscr{C}^\pm(\mathbf{x},c)$ the elasticity tensor and by $\bar{\mathscr{E}}^\pm(\mathbf{x},c)$ the stress-free strains corresponding to the two grains, we require that the equilibrium

https://doi.org/10.1017/S095679250700719X Published online by Cambridge University Press

conditions

$$\nabla \cdot [\mathscr{C}^{\pm}(\mathbf{x},c)(\mathscr{E}(\nabla \mathbf{u}) - \bar{\mathscr{E}}^{\pm}(\mathbf{x},c))] = 0 \qquad \text{in } \Omega^{\pm}, \tag{3.5}$$

$$\mathscr{C}^{\pm}(\mathbf{x},c)(\mathscr{E}(\nabla \mathbf{u}) - \bar{\mathscr{E}}^{\pm}(\mathbf{x},c))v_{\partial\Omega} = \mathscr{S}^{*} v_{\partial\Omega} \qquad \text{on } \partial\Omega^{\pm} \cap \partial\Omega \tag{3.6}$$

have to hold. In addition, on Γ the coherency condition $[\mathbf{u}]_{-}^{+} = 0$ and

$$\mathscr{C}^{+}(\mathbf{x},c)(\mathscr{E}(\nabla \mathbf{u}) - \bar{\mathscr{E}}^{+}(\mathbf{x},c))v = \mathscr{C}^{-}(\mathbf{x},c)(\mathscr{E}(\nabla \mathbf{u}) - \bar{\mathscr{E}}^{-}(\mathbf{x},c))v, \tag{3.7}$$

that is, a balance of normal stresses, have to be fulfilled.

3.2 Non-dimensionalization

In dimensional form, (3.1) can be written as

$$mV = \sigma\kappa + v \cdot [W\,\mathrm{Id} - (\nabla \mathbf{u})^{T}\mathscr{S}]_{-}^{+} v, \tag{3.8}$$

where m is a kinetic coefficient and σ is the surface energy density. Let us shortly describe how we can non-dimensionalize (3.8) and how characteristic length and time scales can be obtained. Taking new non-dimensional quantities $\hat{\mathbf{x}} = \mathbf{x}/l$, $\hat{t} = t/\bar{t}$, $\hat{\mathbf{u}} = \mathbf{u}/(lq)$, $\hat{\mathscr{C}} = \frac{1}{E}\mathscr{C}$ and $\hat{\bar{\mathscr{E}}} = \frac{1}{q}\bar{\mathscr{E}}$, where q represents the typical size of $\bar{\mathscr{E}}$, we obtain from (3.8) that

$$m\frac{l^2}{\sigma\bar{t}}\hat{V} = \hat{\kappa} + \frac{(lq)^2}{l\sigma}Ev \cdot [\hat{W}\,\mathrm{Id} - (\hat{\nabla}\hat{\mathbf{u}})^{T}\hat{\mathscr{S}}]_{-}^{+} v.$$

We now take for E an elastic modulus characterizing the size of the elasticity tensor (e.g. for isotropic elasticity one can take Young's modulus $E = \frac{\mu(2\mu+3\lambda)}{\mu+\lambda}$, where μ, λ are Lamé constants). As appropriate length and time scales, we choose

$$l = \frac{\sigma}{q^2 E} \quad \text{and} \quad \bar{t} = \frac{l^2 m}{\sigma} = \frac{\sigma m}{q^4 E^2},$$

which shows that the misfit parameter q has a strong influence on the scales.

3.3 Explicit solutions of the sharp interface problem

We now discuss explicit solutions to the sharp interface problem. This allows us later to quantitatively compare the numerical solutions of the phase field system with sharp interface solutions. The motion of the free boundary is induced only by stresses if the interface is flat and by stresses and curvature in the radial case. In all of Subsection 3.3, we use an isotropic $\mathscr{C}$, that is

$$\mathscr{C}^{\pm}\mathscr{E} = 2\mu^{\pm}\mathscr{E} + \lambda^{\pm}\mathrm{tr}(\mathscr{E})\mathrm{Id}, \tag{3.9}$$

where $\mu^{\pm}$ and $\lambda^{\pm}$ are the Lamé moduli so that $\mathscr{C}^{\pm} = (2\mu^{\pm} + \lambda^{\pm}, 0, \lambda^{\pm}, \mu^{\pm}, 0, 2\mu^{\pm} + \lambda^{\pm})$; see (2.5). For simplicity we formulate the solution in Subsection 3.3.1 in $\mathbb{R}^2$ but a natural generalization to higher space dimensions is possible.

https://doi.org/10.1017/S095679250700719X Published online by Cambridge University Press

3.3.1 *Longitudinal solutions*

We first consider the case of a vertical boundary spanning the height of $\Omega = (-1,1)^2$ and we take $\lambda^{\pm} = 0$ and

$$\bar{\varepsilon}^{+} = q\mathrm{Id}, \ \bar{\varepsilon}^{-} = 0 \quad \text{and} \quad \mathscr{S}^* = \begin{pmatrix} s^* & 0 \\ 0 & 0 \end{pmatrix}.$$

At initial time we take a straight grain boundary such that $x_1 = 0$. We then obtain a solution that only depends on the first spatial coordinate. Defining by $\gamma(t)$ the x_1-position of the interface at time t, we search for $(u_1, u_2)(x_1, x_2, t) = (v(x_1, t), 0)$, where

$$v(x_1,t) = \begin{cases} v^+(x_1,t) & \text{if} \quad x_1 \geqslant \gamma(t), \\ v^-(x_1,t) & \text{if} \quad x_1 \leqslant \gamma(t). \end{cases}$$

We obtain from (3.5)–(3.7) that

$$\begin{aligned} v^-_{,x} &= \frac{s^*}{\mu^-} && \text{in} \quad (-1, \gamma(t)), \\ v^+_{,x} &= q + \frac{s^*}{\mu^+} && \text{in} \quad (\gamma(t), 1). \end{aligned}$$

The driving force for the interface is then given by (see (3.1))

$$\begin{aligned} V &= \frac{2}{\pi} v \cdot [W\mathrm{Id} - \nabla \mathbf{u}^T \mathscr{S}]^+_- v \\ &= \frac{2}{\pi} \left[\left(\frac{1}{2}\mu^+ \left(\frac{s^*}{\mu^+} \right)^2 - \frac{1}{2}\mu^- \left(\frac{s^*}{\mu^-} \right)^2 \right) + \mu^- \left(\frac{s^*}{\mu^-} \right) \left(\frac{s^*}{\mu^-} \right) - \mu^+ \left(q + \frac{s^*}{\mu^+} \right) \left(\frac{s^*}{\mu^+} \right) \right] \\ &= \frac{2}{\pi} \left(-q s^* - \frac{1}{2}(s^*)^2 \left(\frac{1}{\mu^+} - \frac{1}{\mu^-} \right) \right). \end{aligned}$$

If $\mu^+ = \mu^-$, we obtain an example in which the driving force due to a jump in energy is zero and only the second term in the Eshelby tensor gives a contribution. It is interesting to note that in this case the driving force depends linearly on the elastic misfit parameter q. This is in contrast to the predictions given by the coherency strain theory, where the difference in elastic energy leads to a driving force q, which is quadratic in q (see Handwerker [24] and the references therein).

3.3.2 *Shearing experiment*

Now we would like to construct solutions in which a shearing appears in an isotropic situation with Lamé constants $\lambda^{\pm}$, $\mu^{\pm}$ and stress free strains $\bar{\varepsilon}^{\pm} = 0$. Since we are interested in explicit solutions, we consider a situation with a vertical interface in $\Omega = (-1,1)^3 \subset \mathbb{R}^3$ perpendicular to the x_1-axis, that is

$$\Gamma_t = \{(\gamma(t), x_2, x_3) \mid x_2, x_3 \in (-1,1)\}.$$

We make the ansatz

$$\mathbf{u}(\mathbf{x},t) = \begin{cases} \mathbf{u}^+(\mathbf{x},t) & \text{if} \quad x_1 \geqslant \gamma(t), \\ \mathbf{u}^-(\mathbf{x},t) & \text{if} \quad x_1 \leqslant \gamma(t) \end{cases}$$

https://doi.org/10.1017/S095679250700719X Published online by Cambridge University Press

with

$$\begin{aligned}\mathbf{u}^-(\mathbf{x},t) &= \omega^- x_2 \mathbf{e}_1,\\ \mathbf{u}^+(\mathbf{x},t) &= \omega^- x_2 \mathbf{e}_1 + (\omega^+ - \omega^-)(x_1 - \gamma(t))\mathbf{e}_2.\end{aligned}$$

We then obtain

$$\nabla \mathbf{u}^- = \begin{pmatrix} 0 & \omega^- & 0 \\ 0 & 0 & 0 \\ 0 & 0 & 0 \end{pmatrix}, \ \nabla \mathbf{u}^+ = \begin{pmatrix} 0 & \omega^- & 0 \\ \omega^+ - \omega^- & 0 & 0 \\ 0 & 0 & 0 \end{pmatrix},$$

$$\mathscr{E}^- = \frac{1}{2}\begin{pmatrix} 0 & \omega^- & 0 \\ \omega^- & 0 & 0 \\ 0 & 0 & 0 \end{pmatrix}, \ \mathscr{E}^+ = \frac{1}{2}\begin{pmatrix} 0 & \omega^+ & 0 \\ \omega^+ & 0 & 0 \\ 0 & 0 & 0 \end{pmatrix}$$

and

$$\mathscr{S}^- = \mathscr{C}^- \mathscr{E}^- = \begin{pmatrix} 0 & \mu^-\omega^- & 0 \\ \mu^-\omega^- & 0 & 0 \\ 0 & 0 & 0 \end{pmatrix}, \ \mathscr{S}^+ = \mathscr{C}^+ \mathscr{E}^+ = \begin{pmatrix} 0 & \mu^+\omega^+ & 0 \\ \mu^+\omega^+ & 0 & 0 \\ 0 & 0 & 0 \end{pmatrix},$$

where we recall (3.9) and that $\overline{\mathscr{E}^{\pm}} = 0$. Moreover, the normal stress balance at the interface requires that

$$\mathscr{S}^- \mathbf{e}_1 = \mathscr{S}^+ \mathbf{e}_1 \Rightarrow \mu^-\omega^- = \mu^+\omega^+.$$

Choosing outer stresses of shearing type

$$\mathscr{S}^* = \begin{pmatrix} 0 & s^* & 0 \\ s^* & 0 & 0 \\ 0 & 0 & 0 \end{pmatrix},$$

we have that

$$s^* = \mu^-\omega^- = \mu^+\omega^+.$$

Thus the evolution law for the interface is given by

$$\begin{aligned}\dot{\gamma}(t) = \frac{2}{\pi} v \cdot [W\,\mathrm{Id} - \nabla \mathbf{u}^T \mathscr{S}]^+_- v &= \frac{2}{\pi}\left[\frac{1}{2}(s^*\omega^+ - s^*\omega^-) - (0, \omega^+ - \omega^-, 0)\cdot(0, s^*, 0)^T\right]\\ &= -\frac{2}{\pi}\frac{1}{2}s^*(\omega^+ - \omega^-) = \frac{2}{\pi}\frac{1}{2}(s^*)^2\left(\frac{1}{\mu^-} - \frac{1}{\mu^+}\right).\end{aligned}$$

Since the right-hand side is constant, this implies that we have constructed a travelling wave solution. It is interesting that it is possible to construct a non-trivial travelling wave solution for which $\overline{\mathscr{E}^{\pm}} = 0$, that is no elastic stresses are generated due to an elastic misfit.

3.3.3 *Radially symmetric solutions*

We now choose a radially symmetric situation with $\Omega = B_R(0) \subset \mathbb{R}^d$, where $B_R(0)$ is the ball with radius $R > 0$ and centre 0 in space dimension d. We make the ansatz

$$\Omega_t^- = B_{r(t)}(0), \ \Gamma_t = \partial B_{r(t)}(0), \ \Omega_t^+ = \Omega \setminus \overline{\Omega_t^-}$$

https://doi.org/10.1017/S095679250700719X Published online by Cambridge University Press

and choose $\mathscr{C}^{\pm}$ as in (3.9). Furthermore, let

$$\bar{\mathscr{E}}^{\pm} = q^{\pm}\mathrm{Id}, \quad \mathscr{S}^{*} = s^{*}\mathrm{Id}.$$

For the displacement we make the radially symmetric ansatz

$$\mathbf{u}(\mathbf{x},t) = \mathbf{u}^{\pm}(\mathbf{x},t) = v^{\pm}(|\mathbf{x}|,t)\mathbf{x} \quad \text{if} \quad \mathbf{x} \in \Omega^{\pm}(t),$$

where $v^{\pm}(\rho,t)$, $\rho = |\mathbf{x}|$, are scalar functions to be determined. Since $\bar{\mathscr{E}}^{\pm}$ are constant tensors, the elasticity equations in the bulk give

$$\nabla \cdot (\mathscr{C}^{\pm}(\mathscr{E}(\nabla \mathbf{u}^{\pm}))) = 0 \quad \text{in} \quad \Omega^{\pm}(t).$$

Since we prescribe outer stresses, we obtain

$$\mathscr{C}^{+}(\mathscr{E}(\nabla \mathbf{u}^{+}) - \bar{\mathscr{E}}^{+})\mathbf{x} = s^{*}\mathbf{x} \quad \text{for} \quad \mathbf{x} \in \partial\Omega. \tag{3.10}$$

On the interface we need to fulfil the complementary condition and the stresses have to balance in normal direction, that is we require

$$v^{+}(r(t),t) = v^{-}(r(t),t), \tag{3.11}$$

$$\mathscr{C}^{-}(\mathscr{E}(\nabla \mathbf{u}^{-}) - \bar{\mathscr{E}}^{-})\mathbf{x} = \mathscr{C}^{+}(\mathscr{E}(\nabla \mathbf{u}^{+}) - \bar{\mathscr{E}}^{+})\mathbf{x} \quad \text{for} \quad \mathbf{x} \in \Gamma_t. \tag{3.12}$$

Finally the interface velocity is given by

$$\dot{r}(t) = -\frac{1}{r(t)} + \frac{2}{\pi}\frac{\mathbf{x}}{|\mathbf{x}|} \cdot [W\mathrm{Id} - (\nabla \mathbf{u})^{T}\mathscr{S}]^{+}_{-}\frac{\mathbf{x}}{|\mathbf{x}|} \quad \text{for} \quad \mathbf{x} \in \Gamma_t. \tag{3.13}$$

The functions $\mathbf{u}^{\pm}(\mathbf{x},t) = v^{\pm}(|\mathbf{x}|,t)\mathbf{x}$ are standard radial solutions to the linear elasticity system. We obtain

$$v^{\pm}(\rho,t) = A^{\pm}(t) + B^{\pm}(t)\rho^{-d}.$$

To obtain finite energy solutions we need to require $B^{-}(t) = 0$. We now have to determine A^{+}, B^{+} and A^{-} from (3.10), (3.11) and (3.12), which involve some tedious but straightforward computations. Using the abbreviations

$$f := \frac{1}{2\mu^{+} + d\lambda^{+}} - \frac{1}{2\mu^{-} + d\lambda^{-}}, \quad g := \frac{1}{2\mu^{-} + d\lambda^{-}} + \frac{1}{2\mu^{+}(d-1)},$$

we obtain, on solving a system of three linear equations, that

$$\begin{aligned}
A^{+} &= q^{+} + \frac{1}{(2\mu^{+} + d\lambda^{+})}\frac{1}{(g + f(r^{d}/R^{d}))}\left(gs^{*} + \frac{r^{d}}{R^{d}}(q^{-} - q^{+})\right), \\
A^{-} &= q^{-} + \frac{1}{(2\mu^{-} + d\lambda^{-})}\frac{1}{(g + f(r^{d}/R^{d}))}\left[(f+g)s^{*} + \left(\frac{r^{d}}{R^{d}} - 1\right)(q^{-} - q^{+})\right], \\
B^{+} &= \frac{R^{d}}{2\mu^{+}(1-d)}(s^{*} - (2\mu^{+} + d\lambda^{+})(A^{+} - q^{+})).
\end{aligned}$$

https://doi.org/10.1017/S095679250700719X Published online by Cambridge University Press

For the elastic driving force in the evolution law (3.13) for the radius, we compute

$$\begin{aligned} F(r) &= \frac{2}{\pi}(W^+ - W^- - [v^T(\nabla \mathbf{u})^T \mathscr{S} v]_-^+) \\ &= \frac{2}{\pi}\frac{d}{2}[(2\mu^+ + d\lambda^+)(A^- - q^+)(A^+ - q^+) - (2\mu^- + d\lambda^-)(A^+ - q^-)(A^- - q^-)] \\ &= \frac{2}{\pi}\frac{d}{2}\left(\frac{1}{f(r/R)^d + g}\right)^2 \left\{(q^- - q^+)^2\left(f\left(\frac{r}{R}\right)^{2d} + 2g\left(\frac{r}{R}\right)^d - g\right)\right. \\ &\quad \left. - fg(f+g)(s^*)^2 + 2(f+g)gs^*(q^- - q^+)\right\}, \end{aligned}$$

which is quadratic in $(s^*, q^- - q^+)$. In particular, it is possible that $F(0)$ is positive, which would lead to situations in which the inner phase can grow. This is not possible if we consider pure mean curvature flow that always leads to shrinking inclusions.

We illustrate this with two examples. First, we consider the case of homogeneous elasticity, that is the elasticity tensors $\mathscr{C}^+$ and $\mathscr{C}^-$ are the same, that is $\lambda^\pm = \lambda$, $\mu^\pm = \mu$. For simplicity we choose $R = 1$, $q^- = 0$ and $q^+ = q$, so that (3.13) reads as

$$\dot{r}(t) = -\frac{1}{r} + \frac{2}{\pi}\frac{d}{2}q\left[(2r^d - 1)\frac{q}{g} - 2s^*\right]. \tag{3.14}$$

Choosing q positive and s^* negative, we observe for $(-s^*)$ large enough that a *critical radius* r_{crit} exists, such that radial interfaces will grow if $r(0) > r_{\text{crit}}$ and shrink if $r(0) < r_{\text{crit}}$ (see Figure 2 in Section 5).

In the case $q^- = q^+$, that is in a situation in which no stresses result from an elastic misfit, it is still possible that an inclusion grows. For this to happen, one needs to consider a case of inhomogeneous elasticity, that is $\mathscr{C}^+ \neq \mathscr{C}^-$. We obtain for $R = 1$ that

$$F(r) = \frac{2}{\pi}\frac{d}{2}(s^*)^2(-fg)(f+g)\left(\frac{1}{fr^d + g}\right)^2. \tag{3.15}$$

Since g is positive, we obtain that F is positive in cases where $2\mu^- + d\lambda^- < 2\mu^+ + d\lambda^+$, that is in cases where the "harder" phase is outside (see Figure 4 below).

4 Phase field finite element discretization

In this section we present a semi-implicit discretization of the phase field model derived in Section 2. In this context we refer to [9], where a convergence proof of an explicit method for DIGM has been shown in a situation in which no coupling to an elasticity system appears. The paper by Garcke and Weikard [23] shows convergence of a numerical method for the Cahn–Hilliard equation coupled to an elasticity system. In this paper, we combine the two above approaches to come up with a numerical method for the problem (2.12)–(2.16), which in contrast to the method of [11] will be semi-implicit in the phase field equation and hence allows for larger time steps.

We consider the time interval $[0, T]$ that we subdivide into N steps with length τ_n and set $t_n := \sum_{i=1}^n \tau_i$. In addition, let $t_0 = 0$ and $\tau = \max_{n=1,\dots,N}\{\tau_n\}$. In the following we will assume for simplicity that Ω is a polyhedral domain. Generalizations to curved domains

https://doi.org/10.1017/S095679250700719X Published online by Cambridge University Press

are, of course, possible by using boundary finite elements with curved faces (see, e.g. Ciarlet [8]). Let $\mathscr{T}_h$ be a regular triangulation of Ω into disjoint open simplices, i.e. $\Omega = \cup_{T\in\mathscr{T}_h} \overline{T}$ and no vertex of an element lies in the interior of another element's face. Furthermore, we define $\mathscr{T}_h$ to have maximal element size $h := \max_{T\in\mathscr{T}_h}\{\text{diam } T\}$ and we set J to be the set of nodes of $\mathscr{T}_h$ and $\{p_j\}_{j\in J}$ to be the coordinates of these nodes. Associated with $\mathscr{T}_h$ is the finite element space

$$\mathscr{V}_h := \{\varphi \in C^0(\overline{\Omega}) |\, \varphi_{|_T} \in P_1(T) \;\forall\; T \in \mathscr{T}_h\} \subset H^1(\Omega),$$

where we denote by $P_1(T)$ the set of all affine linear functions on T. To derive a discretization of our model, we set

$$K_h := \{\eta \in \mathscr{V}_h \,|\, |\eta(\mathbf{x})| \leqslant 1 \text{ for all } \mathbf{x} \in \Omega\},$$

and we use the lumped mass scalar product $(\eta,\chi)^h = \int_\Omega I_h(\eta\chi)$ instead of (η,χ), where $I_h : C^0(\overline{\Omega}) \to \mathscr{V}_h$ is the standard interpolation operator such that $(I_h\,\eta)(p_j) = \eta(p_j)$ for all nodes $j \in J$. Similarly, we employ the lumped mass inner product $\langle \mathscr{A},\mathscr{B}\rangle^h_{\mathscr{C}}$ in place of $\langle \mathscr{A},\mathscr{B}\rangle_{\mathscr{C}}$, where we use a quadrature formula that guarantees that $\langle \mathscr{A},\mathscr{B}\rangle^h_{\mathscr{C}} = \langle \mathscr{A},\mathscr{B}\rangle_{\mathscr{C}} = \int_\Omega \mathscr{A} : \mathscr{C}\mathscr{B}$ for piecewise affine linear integrands $\mathscr{A} : \mathscr{C}\mathscr{B}$.

Thus we obtain the following approximation.

4.1 The discrete system

For $n = 1,\dots,N$, and given $c_h^{n-1} \in \mathscr{V}_h$ and $\varphi_h^{n-1} \in K_h$, find $(\varphi_h^n, c_h^n, \mathbf{u}_h^n) \in K_h \times \mathscr{V}_h \times (\mathscr{V}_h)^d$ such that

$$\left\langle \mathscr{E}\left(\nabla \mathbf{u}_h^n\right) - \bar{\mathscr{E}}\left(\mathbf{x}, \varphi_h^{n-1}, c_h^{n-1}\right), \mathscr{E}(\nabla\boldsymbol{\xi})\right\rangle^h_{\mathscr{C}(\varphi_h^{n-1})} = \int_{\partial\Omega} \boldsymbol{\xi}\cdot\mathscr{S}^* v_{\partial\Omega} \quad \forall\; \boldsymbol{\xi} \in (\mathscr{V}_h)^d, \tag{4.1}$$

$$\begin{aligned}
&\varepsilon\left(\frac{\varphi_h^n - \varphi_h^{n-1}}{\tau_n}, \eta - \varphi_h^n\right)^h \\
&\quad\geqslant -\varepsilon\left(\nabla\varphi_h^n, \nabla\left(\eta - \varphi_h^n\right)\right) + \frac{1}{\varepsilon}\left(\varphi_h^n, \eta - \varphi_h^n\right)^h \\
&\qquad - \frac{1}{2}\left\langle \mathscr{E}\left(\nabla\mathbf{u}_h^n\right) - \bar{\mathscr{E}}\left(\mathbf{x},\varphi_h^{n-1},c_h^{n-1}\right), \left(\mathscr{E}\left(\nabla\mathbf{u}_h^n\right) - \bar{\mathscr{E}}\left(\mathbf{x},\varphi_h^{n-1},c_h^{n-1}\right)\right)\left(\eta - \varphi_h^n\right)\right\rangle^h_{\mathscr{C},\varphi(\varphi_h^{n-1})} \\
&\qquad + \left\langle \mathscr{E}\left(\nabla\mathbf{u}_h^n\right) - \bar{\mathscr{E}}\left(\mathbf{x},\varphi_h^{n-1},c_h^{n-1}\right), \bar{\mathscr{E}}_{,\varphi}\left(\mathbf{x},\varphi_h^{n-1},c_h^{n-1}\right)\left(\eta - \varphi_h^n\right)\right\rangle^h_{\mathscr{C}(\varphi_h^{n-1})} \quad \forall\; \eta \in K_h,
\end{aligned} \tag{4.2}$$

and

$$\frac{\varepsilon}{\tau_n}\left(c_h^n - c_h^{n-1}, \chi\right)^h + \left(D\left(\varphi_h^n\right)\nabla c_h^n, \nabla\chi\right) + \alpha\int_{\partial\Omega} I_h\left(D\left(\varphi_h^n\right)\left(c_h^n - 1\right)\chi\right) = 0 \quad \forall\; \chi \in \mathscr{V}_h \tag{4.3}$$

or

$$\varepsilon\left(c_h^n - c_h^{n-1}, \chi - c_h^n\right)^h \geqslant \Lambda\,\tau_n\left(1 - \left(\varphi_h^n\right)^2, \chi - c_h^n\right)^h \quad \forall\; \chi \in \tilde{K}_h, \tag{4.4}$$

where $\tilde{K}_h = \{\eta \in \mathscr{V}_h : 0 \leqslant \eta(\mathbf{x}) \leqslant 1 \;\forall\; \mathbf{x} \in \Omega\}$. For initial data we set $\varphi_h^0 \in K_h$ and $c_h^0 \in \mathscr{V}_h$ to be approximations of the initial data $\varphi_0(\mathbf{x})$ and $c_0(\mathbf{x})$.

https://doi.org/10.1017/S095679250700719X Published online by Cambridge University Press

As (4.1) is independent of (φ_h^n, c_h^n), we use a preconditioned conjugate gradient solver to compute $\mathbf{u}_h^n$ from this equation. We remark that $\mathbf{u}_h^n$ is not unique as we can add any infinitesimal rigid displacement to $\mathbf{u}_h^n$. To obtain a unique $\mathbf{u}_h^n$, we always choose the solution with minimal L^2-norm. We refer to [23] and note that (φ_h^n, c_h^n) are unique since $\mathbf{u}_h^n$ enters (4.1)–(4.4) only through $\mathscr{E}(\nabla \mathbf{u}_h^n)$ and this quantity is uniquely determined. Then the variational inequality (4.2) is solved using a projected SOR method and finally (4.3) and (4.4) are solved with the help of the CG method and a simple projection, respectively. Finally we note that the interfacial thickness is proportional to ε and hence to resolve the interfacial layer we need to choose $h \ll \varepsilon$ (see [10, 11] for details). Away from the interface h can be chosen larger and hence adaptivity in space can heavily speed up computations. In fact we use the finite element toolbox Alberta 1.2 (see Schmidt and Siebert [32]) for adaptivity and we implemented the same mesh refinement strategy as in Barrett *et al.* [3], that is a fine mesh is constructed where $|\varphi_h^{n-1}| < 1$, with a coarser mesh present in the bulk regions $\varphi_h^{n-1} = \pm 1$.

5 Computational experiments

In this section we solve the numerical discretization (4.1)–(4.4) to produce computational experiments of stress and diffusion-induced interface motion. We are predominantly interested in how exterior stresses, an elastic misfit, crystal lattice orientations and structural defects such as dislocations affect the velocity of grain boundaries. Unless it is otherwise stated, we take $\Omega = (-1, 1)^2$, $\varepsilon = \frac{1}{16\pi}$ and a uniform time step size $\tau = 3.125 \times 10^{-5}$. Furthermore, in simulations in which the grain boundary spans Ω, we take initial data such that $\varphi < 0$ to the left of the boundary and $\varphi > 0$ to the right, while in simulations where the grain boundary is a closed curve, we take $\varphi > 0$ in the exterior of the curve and $\varphi < 0$ in the interior.

We always choose $\mathscr{C}$ to be of the form (2.3). In most experiments we assume that stresses are generated by an atomic misfit, which, for example in the case of DIGM is generated by the solute in the solvent lattice and we mainly choose

$$\bar{\mathscr{E}} = cq\,\mathrm{Id} \quad \text{or} \quad \bar{\mathscr{E}} = \frac{q}{2}(1+\varphi)\,\mathrm{Id} \qquad q \in \mathbb{R}.$$

For the first choice the atomic misfit is caused by the solvent. The second choice is, for example, appropriate when studying thin films in which the whole of one grain already contains the solute. In subsections 5.1–5.6 we consider a thin film set-up in which the concentration c is a solution of equation (4.4) with $\Lambda = 100$. Furthermore, in Subsections 5.1–5.3 we take $\bar{\mathscr{E}} = \frac{q}{2}(1+\varphi)\mathrm{Id}$ while in Subsections 5.4 and 5.5 we take $\bar{\mathscr{E}} = cq\mathrm{Id}$. The simulations in Subsections 5.4–5.7 are relevant for DIGM as they show how the presence of a solvent can drive the motion of a grain boundary.

5.1 Numerical approximation of explicit sharp interface solutions

In this subsection we neglect the c-dependence in the phase field variational inequality in (2.12) and in the elasticity system (2.14). The system then models grain boundary motion under external stresses. We remark that in these comparisons two errors have to

https://doi.org/10.1017/S095679250700719X Published online by Cambridge University Press

Table 1. *Comparison with the longitudinal sharp interface solutions:* $s^* = 1$.

q	1	2	3	4
$\frac{\pi}{2} V_{\text{th}}$	1	2	3	4
$\frac{\pi}{2} V_{\text{comp}}$	0.9972414	1.993543	2.991971	3.990194

Table 2. *Comparison with the longitudinal sharp interface solutions:* $q = 1$.

s^*	-1	-2	-3	-4
$\frac{\pi}{2} V_{\text{th}}$	1	2	3	4
$\frac{\pi}{2} V_{\text{comp}}$	0.9985159	1.993361	2.969894	3.98218

Table 3. *Comparison with the longitudinal sharp interface solutions:* $s^* = -2$, $q = 1$.

ε	$\frac{1}{4\pi}$	$\frac{1}{8\pi}$	$\frac{1}{16\pi}$
$\frac{\pi}{2} V_{\text{comp}}$	1.981181	1.990840	1.998328

be accounted for. One stems from a difference between the sharp interface solution and the phase field solution, and the second comes from the discretization of the phase field equation.

5.1.1 *Longitudinal experiments*

In Tables 1 and 2 and in the left hand and centre plots of Figure 1, we report on numerical experiments for the phase field system that approximates the sharp interface solutions in Subsection 3.3.1. In Figure 1 we show two simulations obtained with the parameters $\mu^{\pm} = 1$, $s^* = -2$, $q = 1$ (left-hand simulation) and $\mu^{\pm} = 1$, $s^* = 1$, $q = 4$ (centre simulation). In the left-hand simulation the grain boundary is initially positioned to the left of the domain at $x_1 = -0.65$ and as time evolves it moves to the right, whereas in the centre simulation the grain boundary is initially placed to the right of the domain at $x_1 = 0.65$ and as time evolves it moves to the left. In both simulations the grain boundary is shown at times $t = 0, 0.1, \ldots, 0.5$. Hence motion in different directions is observed. The velocity of the interface agrees well with the exact sharp interface solution (see Tables 1 and 2), in which the theoretical velocity V_{th} and computational velocity V_{comp} of the grain boundary at $t = 0.1$ are given for different values of q and s (in these experiments we took $\tau = 3.125 \times 10^{-6}$).

To demonstrate this issue in more detail, we present results for different ε in Table 3, which shows the computational velocity $\frac{\pi}{2} V_{\text{comp}}$ of the grain boundary at $t = 0.1$ for $s^* = 2$ and $q = 1$ and hence the theoretical speed $\frac{\pi}{2} V_{\text{th}} = 2.0$. In particular, we see that the sharp interface is resolved more accurately as ε and τ decrease, for the computations $\varepsilon = \frac{1}{4\pi}$, $\varepsilon = \frac{1}{8\pi}$ and $\varepsilon = \frac{1}{16\pi}$, we took $\tau = 3.125 \times 10^{-5}$, $\tau = 3.125 \times 10^{-6}$ and $\tau = 3.125 \times 10^{-7}$,

https://doi.org/10.1017/S095679250700719X Published online by Cambridge University Press

Table 4. *Shearing experiments: Comparison with analytic solutions in the case* $q = 0$.

	$s^* = -4$ $\mu^- = 2,\ \lambda^- = 2$ $\mu^+ = 1,\ \lambda^+ = 1$	$s^* = -1$ $\mu^- = 1,\ \lambda^- = 1$ $\mu^+ = 3,\ \lambda^+ = 2$	$s^* = 2$ $\mu^- = 1,\ \lambda^- = 2$ $\mu^+ = 2,\ \lambda^+ = 2$	$s^* = 2$ $\mu^- = 5,\ \lambda^- = 5$ $\mu^+ = 1,\ \lambda^+ = 1$
$\frac{\pi}{2} V_{\text{th}}$	-4	$\frac{1}{3}$	1	-1.6
$\frac{\pi}{2} V_{\text{comp}}$	-4.027478	0.3321723	0.999461	-1.608778

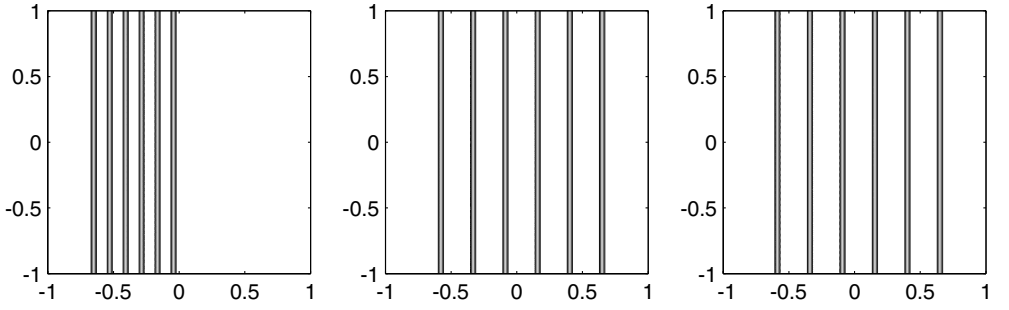


FIGURE 1. Longitudinal experiment with $q = 1,\ s^* = -2$ (left), $q = 4,\ s^* = 1$ (centre), shearing experiment $s^* = -4,\ \mu^+ = \lambda^+ = 1,\ \mu^- = \lambda^- = 2$ (right).

respectively. We note that the entries in Tables 1–3 are $\frac{\pi}{2} V_{\text{comp}}$ and $\frac{\pi}{2} V_{\text{th}}$ and not the actual velocities V_{comp} and V_{th}.

5.1.2 *Shearing experiments*

In Table 4 and the right-hand simulation in Figure 1, we report on numerical experiments for the phase field system that approximates the sharp interface solutions in Subsection 3.3.2. In Figure 1, we show a simulation obtained with the parameters $s^* = -4$, $\mu^+ = \lambda^+ = 1,\ \mu^- = \lambda^- = 2$. The grain boundary is initially positioned to the right of the domain at $x_1 = 0.65$ and as time evolves it moves to the left (the grain boundary is shown at $t = 0, 0.1, \ldots, 0.5$). Again we see that the velocity of the interface agrees well with the exact sharp interface solution; see Table 4 in which the theoretical velocity V_{th} and computational velocity V_{comp} of the grain boundary at $t = 0.1$ are given for different values of s^*, μ^+ and μ^-. In these experiments we took $\tau = 3.125 \times 10^{-7}$. We note that as above the entries in Table 4 are $\frac{\pi}{2} V_{\text{comp}}$ and $\frac{\pi}{2} V_{\text{th}}$ and not the actual velocities V_{comp} and V_{th}.

5.1.3 *Radially symmetric solutions*

In the first set of computations (see Figures 2 and 3), we report on numerical experiments for the phase field system that approximates the sharp interface solutions in Subsection 3.3.3; we consider the radially symmetric case of a circular domain Ω with centre the origin and radius 1 and an initial interface of a circle with radius 0.6 and centre the origin. Furthermore, we take $q = 1,\ \mu^{\pm} = \lambda^{\pm} = 1$ (compare (3.9)), $\mathscr{S}^* = s^* \mathrm{Id}$ and $\tau = 3.125 \times 10^{-6}$.

https://doi.org/10.1017/S095679250700719X Published online by Cambridge University Press

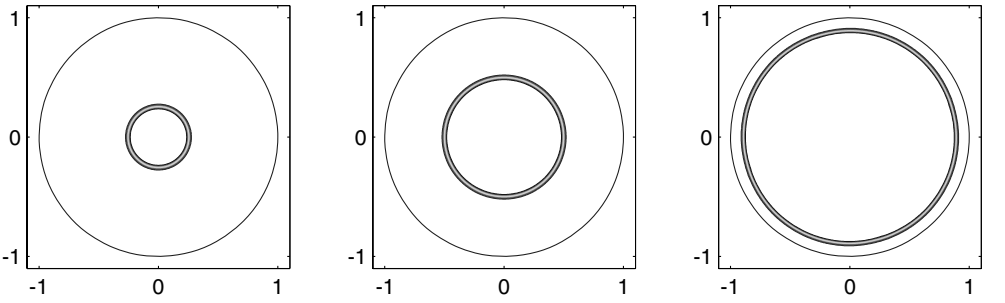


FIGURE 2. Radially symmetric solutions with $s^* = -1$ (left-hand plot), $s^* = -1.496$ (centre plot) and $s^* = -5$ (right-hand plot).

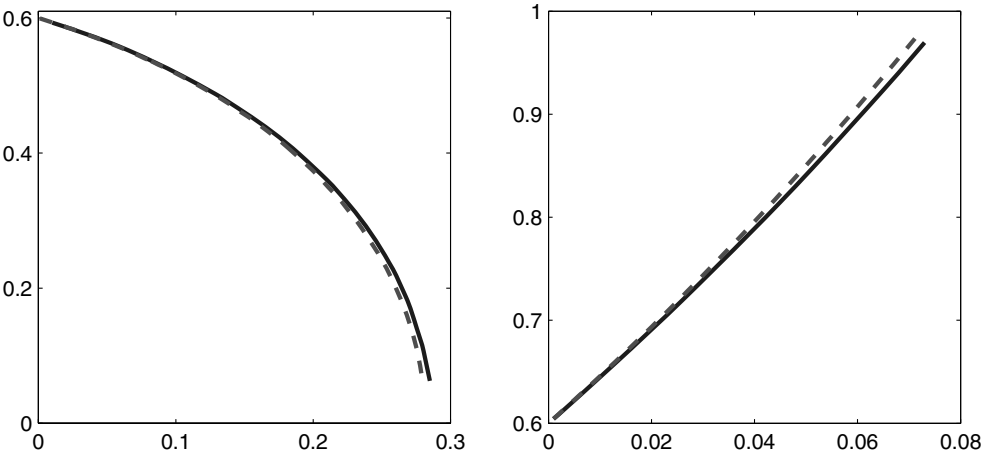


FIGURE 3. Comparison of numerical experiments with explicit radially symmetric solutions.

For the chosen values it is easily established from (3.14) that for a critical radius $r_{\text{crit}} = 0.6$, s^* satisfies $s^* = \frac{4}{3}(2(0.6)^2 - 1) - \frac{\pi}{4}\frac{1}{0.6} = -1.496$.

In Figure 2 we show numerical experiments for three values of s^*; $s^* = -1$ (left-hand plot), $s^* = -1.496$ (centre plot) and $s^* = -5$ (right-hand plot). In the left-hand plot we show the solution at time $t = 0.25$ and we see that the radius of the circular interface has shrunk from 0.6 to 0.257, which is what is predicted by (3.14). Similarly, in the right-hand plot we show the solution at $t = 0.056$, where the circular interface has grown from 0.6 to 0.875. In the centre plot we show the solution at $t = 0.1$ and since we start with the critical radius as predicted the circular interface remains at this radius.

In Figure 3 we set $s^* = -1$ (left-hand plot) and $s^* = -5$ (right-hand plot) and for each value of s^* we plot the solution r of (3.14) against t (dashed line) and compare it with the radius of the numerical experiment plotted against t (bold line). We note that we do not plot values of r up to $r = 0$ or $r = 1$ (the radius of Ω) since for the phase field computation we will experience errors as the interfacial region shrinks to a point or reaches the outer boundary.

https://doi.org/10.1017/S095679250700719X Published online by Cambridge University Press

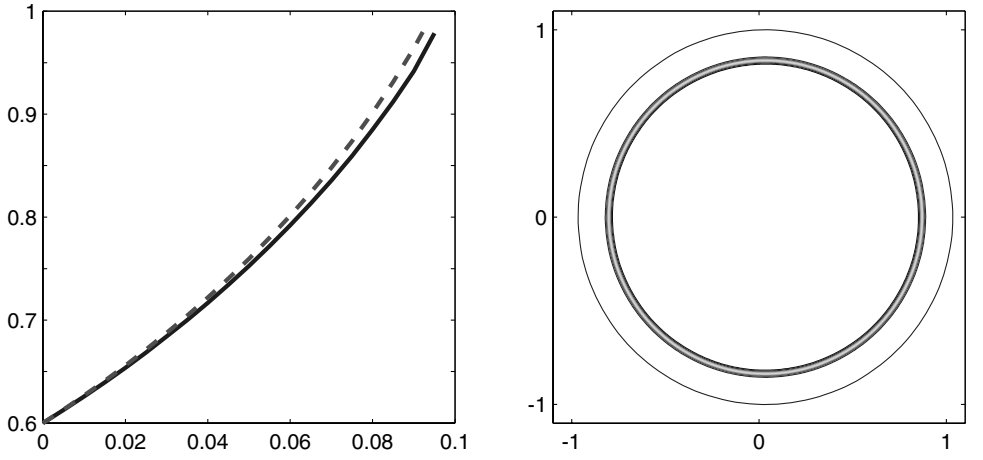


FIGURE 4. Comparison of numerical experiments with explicit radially symmetric solutions.

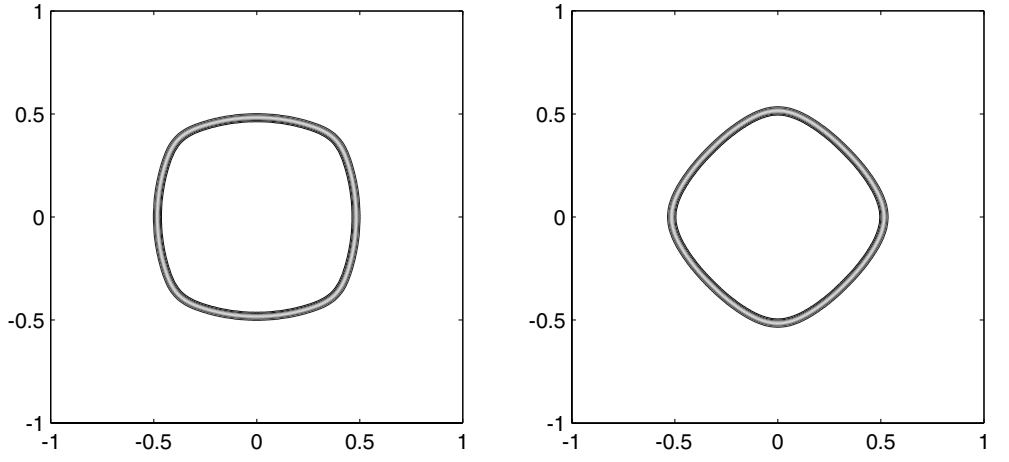


FIGURE 5. Static solutions for anisotropic constant elasticity tensors $\mathscr{C}$ with external stresses $\mathscr{S}^*$.

In the case $q^- = q^+$, that is in a situation in which no stresses result from an elastic misfit, it is still possible that an inclusion grows. For this to happen, one needs to consider a case of inhomogeneous elasticity, that is $\mathscr{C}^+ \neq \mathscr{C}^-$. In Figure 4 we set $s^* = 7$ and consider the situation of inhomogeneous elasticity ($\lambda^+ = \mu^+ = 3$, $\lambda^- = \mu^- = 1$) with no stresses resulting from an elastic misfit ($q^\pm = 0$). In the left-hand figure we plot the solution r of (3.15) against t (dashed line) and compare it with the radius of the numerical experiment plotted against t (bold line), while in the right-hand figure we show the solution at $t = 0.07$, where the circular interface has grown from 0.6 to 0.8356.

5.2 Anisotropic elasticity

Similar results to the one in the centre subplot of Figure 2 can be obtained for anisotropic elasticity tensors. The computations in Figure 5 show stationary solutions that are obtained

https://doi.org/10.1017/S095679250700719X Published online by Cambridge University Press

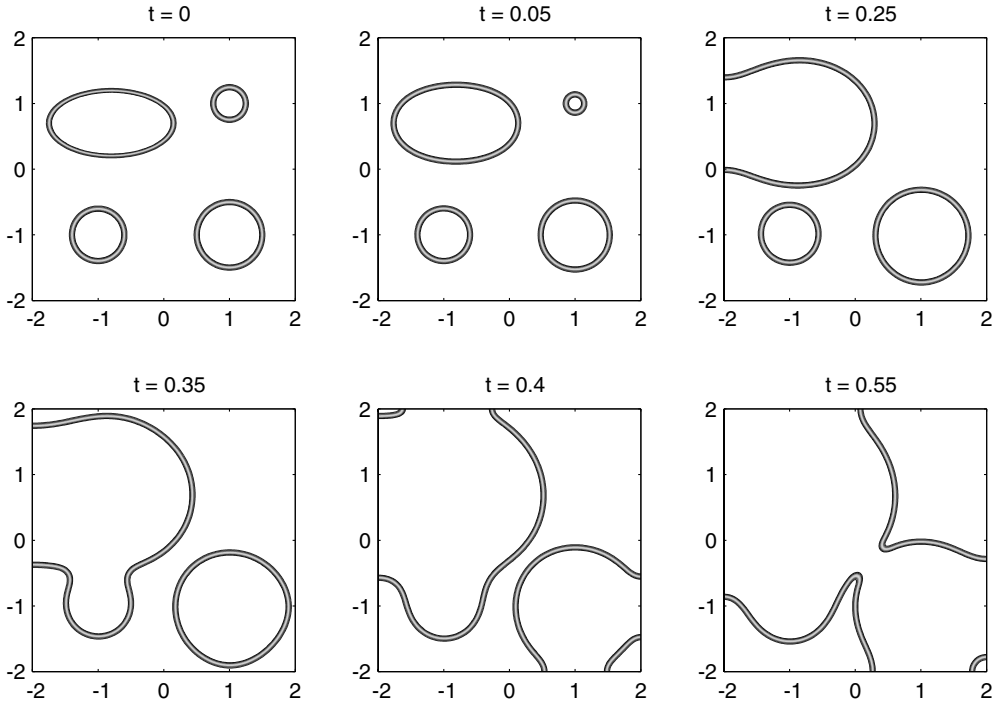


FIGURE 6. Isotropic constant $\mathscr{C}$ with external stresses $\mathscr{S}^*$, particles above a critical size grow.

using an elasticity tensors with cubic anisotropy together with specific choices of $\mathscr{S}^*$. In the left-hand subplot we took $\mathscr{C}^{\pm} = (28, 0, 27, 27, 0, 28)$ with $\mathscr{S}^* = -2.2\mathrm{Id}$ while in the right-hand plot $\mathscr{C}^{\pm} = (28, 0, 1, 1, 0, 28)$ with $\mathscr{S}^* = -2.4\mathrm{Id}$. These choices of the elasticity tensor correspond to the cases of positive and negative anisotropy (see [16]). We remark that smaller inclusions will shrink and larger inclusions will grow also in this anisotropic situation.

5.3 Recrystallization and critical sizes of nuclei

In Figure 6 we give an example on how outer stresses influence the recrystallization of grain boundaries. We set $\mathscr{S}^* = -2.4\mathrm{Id}$ and $q = 1$ and we start with four grains of different sizes in a domain $\Omega = (-2, 2)^2$. We see that the grains either shrink or grow depending on the size. As in models for solidification also in stress-induced interface motion a critical size of phase nuclei seems to be crucial for growth.

5.4 Diffusion and lattice rotation-induced grain boundary motion

To simulate situations in which a grain boundary separates two crystal lattices that differ by a rotation, we take specific choices of $\mathscr{C}^-$ and $\mathscr{C}^+$ in the elasticity tensor (2.3); see (5.1) below. We represent a lattice rotation in $\mathbb{R}^3$ with the help of the rotation axis that is given by the direction of a unit vector $\rho = (\rho_1, \rho_2, \rho_3)$ and an angle θ, which describes the rotation in a clockwise sense about the axis given by ρ. In matrix form, the linear

https://doi.org/10.1017/S095679250700719X Published online by Cambridge University Press

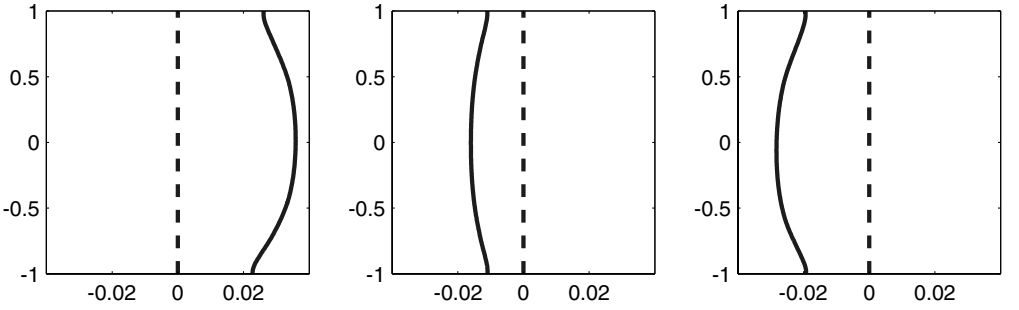


FIGURE 7. Lattice rotations with $\theta^+ = \frac{\pi}{8}$ and $\theta^- = 0$ (left), $\theta^- = \frac{\pi}{6}$ (centre) and $\theta^- = \frac{\pi}{4}$ (right) at $t = 0$ and $t = 0.1$.

mapping R related to the rotation is given by (see Sutton and Balluffi [33, p. 9])

$$R = \rho \otimes \rho + \cos\theta(\mathrm{Id} - \rho \otimes \rho) + (\sin\theta)\rho\times,$$

where $M = \rho\times$ is a skew symmetric mapping defined via $Mv = \rho \times v$ for all $v \in \mathbb{R}^3$. We use the notation $(\rho \otimes \rho)\, v = (\rho \cdot v)\rho$, $(\rho \times v) = (\rho_2 v_3 - \rho_3 v_2, \rho_3 v_1 - \rho_1 v_3, \rho_1 v_2 - \rho_2 v_1)$.

We now assume that $\tilde{\mathscr{C}}$ is a given elasticity tensor with cubic anisotropy with respect to one given reference orientation of the lattice. Given the rotations R^-, R^+ related to the two grains, we can compute the elasticity tensors by the usual rule for fourth rank tensors, that is for $R^\pm = (r^\pm_{ij})_{i,j=1,2,3}$, we obtain

$$\mathscr{C}^\pm_{ijkl} = \sum_{m,n,p,q=1}^{3} r^\pm_{im} r^\pm_{jn} r^\pm_{kp} r^\pm_{lq} \tilde{\mathscr{C}}_{mnpq}. \tag{5.1}$$

For a rotation $R^\pm$ we denote a unit vector related to the rotation axis and the corresponding angle of rotation by $\rho^\pm$ and $\theta^\pm$, respectively. Our simulations will always be in two spatial dimensions. We compute $\mathscr{C}^\pm$ by the formula (5.1) and use only the components $\mathscr{C}^\pm_{ijkl}$ with $i, j, k, l \in \{1, 2\}$.

In Figure 7 we see how the angle of rotation θ^- affects the direction in which the boundary moves. For initial data we take a single interface positioned in the centre of the domain (i.e. at $x_1 = 0$). We set $q = 2$, $\mathscr{S}^* = 0$, $\rho^\pm = (0, 0, 1)$, $\tilde{\mathscr{C}} = (4, 0, 1, 1, 0, 4)$ and $\theta^+ = \frac{\pi}{8}$. In the three subplots we display the zero-level line of φ at times $t = 0$ (dashed line) and $t = 0.1$ (bold line) for $\theta^- = 0$ (left-hand plot), $\theta^- = \frac{\pi}{6}$ (centre plot) and $\theta^- = \frac{\pi}{4}$ (right-hand plot). We see that the direction of the motion depends on θ in the following way: when $\theta^+ > \theta^-$ the interface moves to the right (i.e. the grain that is associated with lattice orientation θ^+ advances into the grain associated with lattice orientation θ^-), whereas for $\theta^+ < \theta^-$ the interface moves to the left (i.e. the grain that is associated with lattice orientation θ^- advances into the grain associated with lattice orientation θ^+). We also see that the value of θ^- has quite a large effect on the initial velocity of the interface, since the interface moves almost twice as far for $\theta^- = 0$ and $\theta^- = \frac{\pi}{4}$ as it does for $\theta^- = \frac{\pi}{6}$. To see this effect in more detail we repeated the experiment for $\theta^- = \frac{n\pi}{24}$, $n = 0, 1, 2, \ldots, 24$ and

https://doi.org/10.1017/S095679250700719X Published online by Cambridge University Press

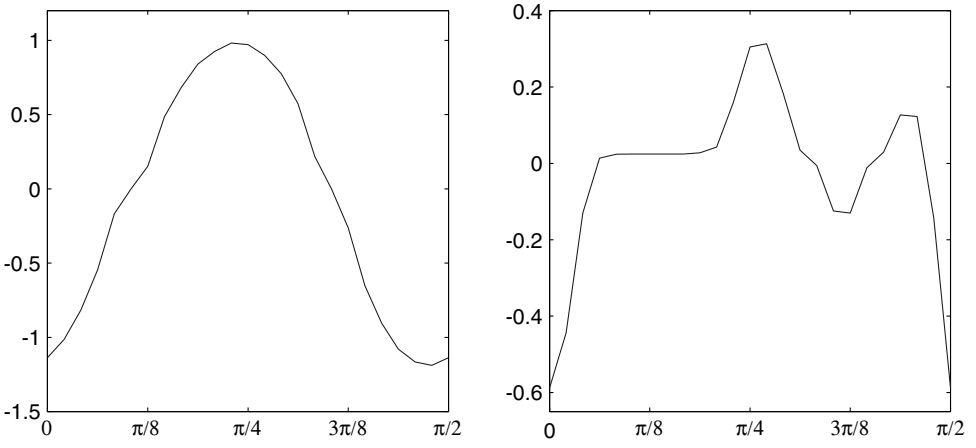


FIGURE 8. Dependence on angle rotation.

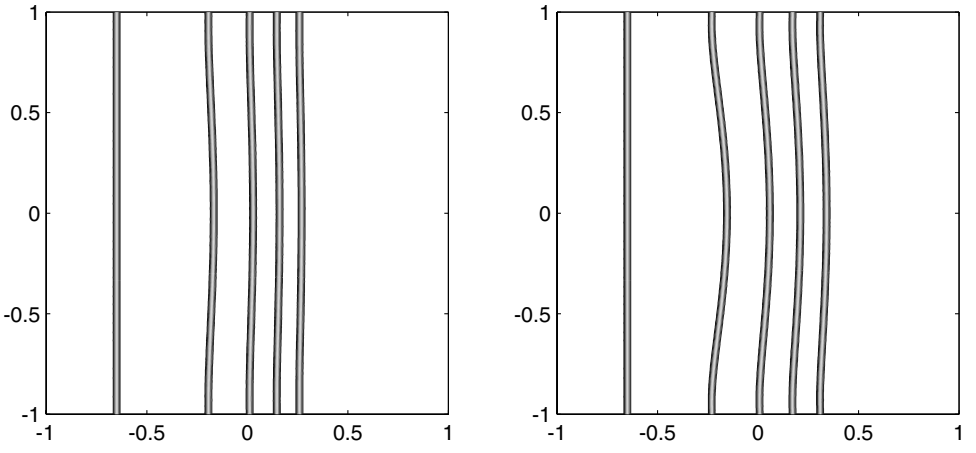


FIGURE 9. q^2 dependence.

in the left-hand plot of Figure 8 we plot the velocity of the interface at $t = 0.1$ against the angle of rotation θ^-. The right-hand plot takes the same form as the left-hand plot one except that here we took $q = 0$ and $\mathscr{S}^* = 20\mathrm{Id}$. As $\theta^+ = \frac{\pi}{8}$ we clearly see a difference between low-angle and large-angle grain boundaries (see [33]).

5.5 Dependence on q

In Figure 9 we show the effect that q has on the speed of the interface. To this end, we consider the motion of a single interface that spans the domain and is positioned at $x_1 = -0.65$. In each simulation we took $\rho^{\pm} = (0, 0, 1)$, $\tilde{\mathscr{C}} = (4, 0, 1, 1, 0, 4)$, $\theta^+ = 0$ and $\theta^- = \frac{\pi}{4}$. In the simulation on the left, which shows the position of the grain boundary at times $t = 0, 2, \ldots, 8$, we took $q = 2$, while in the simulation on the right, which shows the position of the grain boundary at times $t = 0, 0.5, \ldots, 2$, we took $q = 4$. The coherency

https://doi.org/10.1017/S095679250700719X Published online by Cambridge University Press

Table 5. *Time taken for the interface to move* 3 *given distances for* 3 *values of* q.

q	1	2	4
$\delta = 0.2$	2.38	0.66	0.20
$\delta = 0.4$	6.30	1.62	0.47
$\delta = 0.6$	13.34	3.27	0.85

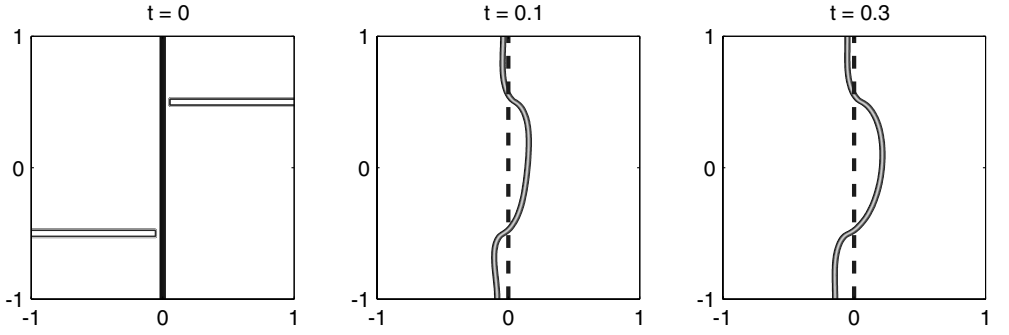


FIGURE 10. A dislocation.

strain theory (cf. Handwerker [24]) states that the velocity depends quadratically on q, which is approximately fulfilled in Figure 9. We also see that the velocity of the boundary is not uniform with time. So in order to study the dependence of q in more detail, we study the time taken for the boundary to move a given distance rather than the velocity of the boundary at given times. In Table 5, we show the time taken, t, in order for the grain boundary to travel distances $\delta = 0.2$, 0.4 and 0.6 for different values of q. From this table we see that the dependence of the velocity is not exactly q^2 but it is roughly of this order. This can, for example, result from curvature effects.

5.6 Dislocation-induced interface motion

In Figure 10 we set

$$\bar{\varepsilon} = \bar{\varepsilon}^d + \bar{\varepsilon}^i,$$

where

$$\bar{\varepsilon}^d = \begin{pmatrix} \frac{1}{2}b & 0 \\ 0 & \frac{1}{2}b \end{pmatrix} \quad \text{and} \quad \bar{\varepsilon}^i = \frac{1}{2}(1+\varphi)\mathrm{Id}$$

with

$$b = \begin{cases} \frac{1}{2\varepsilon} & \text{for all } (x_1, x_2) : \ x_1 < -0.05, \ |x_2 + 0.5| < \varepsilon \ \text{ and } \ x_1 > 0.05, \ |x_2 - 0.5| < \varepsilon, \\ 0 & \text{otherwise.} \end{cases}$$

Here the term $\bar{\varepsilon}^d$ in the stress-free strain is used to simulate edge dislocations in Ω (see [25]). We start with an initially straight interface positioned at $x_1 = 0$, see left-hand plot,

https://doi.org/10.1017/S095679250700719X Published online by Cambridge University Press

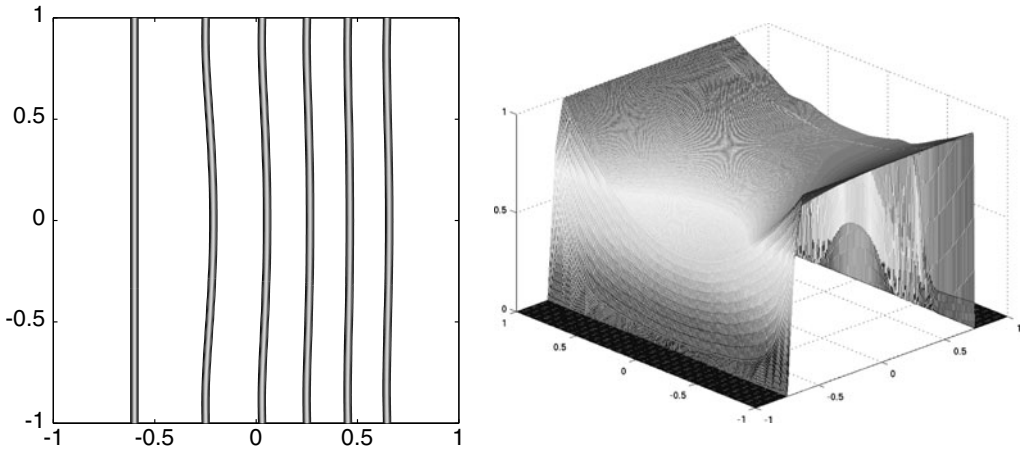


FIGURE 11. Thick film experiment with $\theta^+ = 0$, $\theta^- = \frac{\pi}{4}$, $\tilde{\mathscr{C}} = (4, 0, 1, 1, 0, 4)$ and $\rho^\pm = (0, 0, 1)$.

in which the position of the interface is displayed together with the support of b. We see from the two remaining plots that as time evolves the interface curves dramatically at the two points where it is closest to the edge dislocations. We clearly see that bidirectional motion can be caused by dislocations. Of course, for this computation we adapted the previously described mesh refinement procedure so that a fine mesh is present in the regions where the dislocation occurs.

5.7 Thick film simulations

We conclude the computational results with Figure 11, in which the concentration c is a solution of the diffusion equation (2.13) and $\bar{\mathscr{E}} = cq\mathrm{Id}$, with $q = 4$, $S^* = 0$, $D_c = \frac{1}{7}$ and $\alpha = 100$. We simulate the situation in which a grain boundary separates two crystal lattices that differ by a rotation of $\frac{\pi}{4}$, in particular we take $\rho^\pm = (0, 0, 1)$, $\tilde{\mathscr{C}} = (4, 0, 1, 1, 0, 4)$, $\theta^+ = 0$ and $\theta^- = \frac{\pi}{4}$. In the left-hand plot we display the position of the grain boundary at $t = 0, 1, 2, 3, 4, 5$ while in the right-hand plot we display the concentration at $t = 5$.

Conclusions

We introduced a phase field model for stress and diffusion-induced interface motion. In particular, the model can be used to describe the motion of grain boundaries in the presence of diffusion in the interface as well as interfacial and elastic energy effects. In contrast to earlier work on diffusion-induced grain boundary motion, here we incorporate the elasticity system into the phase field model, which leads to a more accurate approximation.

Using formal asymptotics, we derived the sharp interface problem related to this phase field model. For the sharp interface model we constructed several new explicit solutions. In addition, we introduced a suitable finite element discretization for the phase field model. The numerical method was tested with the help of the obtained true sharp interface solutions. Finally, the numerical simulations demonstrate several phenomena

https://doi.org/10.1017/S095679250700719X Published online by Cambridge University Press

that can be described with the help of our model, including bidirectional motion caused by dislocations.

Appendix: Deriving the sharp interface problem

In this Appendix we outline how one can derive the sharp interface problem (3.1)–(3.7) from the phase field model using the method of matched asymptotic expansions. We refer to the papers [2, 13, 14, 17, 21, 27] for more details about this method. Obtaining the equations in the bulk is straightforward and we discuss only the derivation of the equations on the interface. In what follows we restrict ourselves to two space dimensions although a straightforward generalization to higher-space dimensions is possible.

Let $\Gamma_t \subset \mathbb{R}^2$ be the sharp interface at time t. Let ν be the unit normal to Γ_t pointing into Ω^+. We choose a unit tangent vector τ such that (ν, τ) is positively orientated. Close to the interface we choose a new coordinate system $(s(\mathbf{x}, t), \rho(\mathbf{x}, t))$, where s is an arclength parameter on Γ_t and $\rho = d/\varepsilon$, where $d(\mathbf{x}, t)$ is the signed distance of $\mathbf{x}$ to Γ_t. For the variables $(\varphi, c, \mathbf{u})$ we carry out, close to the interface, an asymptotic expansion in ε in the new coordinates. For example, for $\mathbf{u}$ we get the ansatz

$$\mathbf{u}(\mathbf{x}, t) = \mathbf{U}(\rho, s, t) = \mathbf{U}_0(\rho, s, t) + \varepsilon \mathbf{U}_1(\rho, s, t) + \cdots.$$

In the new coordinates we obtain (compare [21, 2])

$$\begin{aligned} \nabla_x \mathbf{u}(\mathbf{x}, t) &= \frac{1}{\varepsilon} \partial_\rho \mathbf{U} \otimes \nu + \partial_s \mathbf{U} \otimes (\tau + \mathcal{O}(\varepsilon)), \\ \nabla_x \cdot \mathbf{u}(\mathbf{x}, t) &= \frac{1}{\varepsilon} (\partial_\rho \mathbf{U}) \cdot \nu + \partial_s \mathbf{U} \cdot (\tau + \mathcal{O}(\varepsilon)) \end{aligned}$$

and since $V = -\partial_t d$ we have

$$\partial_t \varphi = -\frac{1}{\varepsilon} V \partial_\rho \Phi + \mathcal{O}(1).$$

We will also need the following matching conditions between the inner solution $\mathbf{U}$ and the outer solution $\mathbf{u} = \mathbf{u}_0 + \varepsilon \mathbf{u}_1 + \cdots$: As $\rho \to \pm\infty$

$$\mathbf{U}_0(\rho, s, t) \approx \mathbf{u}_0(\mathbf{x} \pm 0, t), \tag{5.2}$$

$$\mathbf{U}_1(\rho, s, t) \approx \mathbf{u}_1(\mathbf{x} \pm 0, t) + (\nabla \mathbf{u}_0(\mathbf{x} \pm 0, t)\nu)\rho, \tag{5.3}$$

$$\partial_\rho \mathbf{U}_1(\rho, s, t) \approx \nabla \mathbf{u}_0(\mathbf{x} \pm 0, t)\nu \tag{5.4}$$

where $\mathbf{U}_0, \mathbf{U}_1$ are from the inner expansion at a point $\mathbf{x} \in \Gamma_t$ and

$$\mathbf{u}(\mathbf{x} \pm 0, t) = \lim_{\delta \to 0+} \mathbf{u}(\mathbf{x} \pm \delta \nu, t).$$

We now write equations (2.8), (2.9), (2.11) and the variational inequality (2.12) in the inner variables and expand everything in ε. We treat the variational inequality with the help of an approach introduced in [2]. It is required that the variational inequality (2.12) is true for all

$$\eta = \eta_0 + \varepsilon \eta_1 + \varepsilon^2 \eta_2 + \cdots$$

https://doi.org/10.1017/S095679250700719X Published online by Cambridge University Press

which are assumed to have to all order values in $[-1,1]$. To the order $\frac{1}{\varepsilon}$, we obtain that

$$0 \geqslant -(\partial_\rho \Phi_0, \partial_\rho(\eta_0 - \Phi_0)) + (\Phi_0, \eta_0 - \Phi_0) \quad \text{in} \quad \mathbb{R}.$$

Up to translations we obtain the unique solution

$$\Phi_0(\rho) = \begin{cases} 1 & \text{if} \quad \rho > \dfrac{\pi}{2}, \\ \sin\rho & \text{if} \quad \rho \in \left[-\dfrac{\pi}{2}, \dfrac{\pi}{2}\right], \\ -1 & \text{if} \quad \rho < -\dfrac{\pi}{2}. \end{cases}$$

The diffusion equations (2.8), (2.9) give to leading order $\partial_\rho(D(\Phi_0)\partial_\rho \mathbf{C}_0) = 0$, where $D(\Phi_0) > 0$ in the interfacial region. Hence $D(\Phi_0)\partial_\rho \mathbf{C}_0$ is constant and the continuity of fluxes implies that $D(\Phi_0)\partial_\rho \mathbf{C}_0 = 0$, and therefore we obtain that $\mathbf{C}_0$ is constant.

For the elasticity system we obtain to leading order (in the following we will not state the dependence on φ, c explicitly)

$$\left[W_{,\mathscr{E}\mathscr{E}}\left(\mathscr{E}\left(\frac{1}{\varepsilon}\partial_\rho \mathbf{U}_0 \otimes \nu\right)\right)\right] \mathscr{E}(\partial_{\rho\rho}\mathbf{U}_0 \otimes \nu) = 0.$$

Strict coercivity of W implies that $W_{,\mathscr{E}\mathscr{E}}$ is invertible and hence

$$\mathscr{E}(\partial_{\rho\rho}\mathbf{U}_0 \otimes \nu) = 0,$$

which gives $\partial_{\rho\rho}\mathbf{U}_0 = 0$ and matching implies that $\mathbf{U}_0$ is bounded and hence constant. We, therefore, obtain using the matching condition (5.2) that $[\mathbf{u}]_-^+ = 0$. We now get

$$\begin{aligned} \mathscr{E}(\mathbf{U}) &= \mathscr{E}(\partial_\rho \mathbf{U}_1 \otimes \nu + \partial_s \mathbf{U}_0 \otimes \tau) + \mathscr{O}(\varepsilon), \\ W_{,\mathscr{E}}(\mathscr{E}(\mathbf{U})) &= W_{,\mathscr{E}}(\mathscr{E}(\partial_\rho \mathbf{U}_1 \otimes \nu + \partial_s \mathbf{U}_0 \otimes \tau)) + \mathscr{O}(\varepsilon). \end{aligned}$$

Hence the stress balance (2.11) gives to order $\mathscr{O}(\frac{1}{\varepsilon})$

$$\partial_\rho W_{,\mathscr{E}}(\mathscr{E}(\partial_\rho \mathbf{U}_1 \otimes \nu + \partial_s \mathbf{U}_0 \otimes \tau))\nu = 0. \tag{5.5}$$

The matching conditions (5.2) and (5.3) imply that for $\rho \to \pm\infty$ we obtain from matching (not stating the t-dependence in an explicit way)

$$\partial_\rho \mathbf{U}_1 \otimes \nu + \partial_s \mathbf{U}_0 \otimes \tau \to (\nabla \mathbf{u}_0(\mathbf{x} \pm 0)\nu) \otimes \nu + (\partial_\tau \mathbf{u}_0(\mathbf{x} \pm 0)) \otimes \tau = \nabla \mathbf{u}_0(\mathbf{x} \pm 0). \tag{5.6}$$

Hence (5.5) and (5.6) give

$$W_{,\mathscr{E}}(\mathscr{E}(\nabla \mathbf{u}_0(\mathbf{x} + 0)))\nu = W_{,\mathscr{E}}(\mathscr{E}(\nabla \mathbf{u}_0(\mathbf{x} - 0)))\nu,$$

which is the continuity of normal stresses. The major task is now to derive the kinetic law (3.1).

Plugging the asymptotic expansions into the variational inequality (2.12) and taking

$$\eta = \eta_0 + \varepsilon\eta_1 + \cdots,$$

https://doi.org/10.1017/S095679250700719X Published online by Cambridge University Press

which is assumed to have to all orders values in $[-1,1]$, gives (where we always extend $\mathbf{C}_0(\cdot,s,t)$ constant to the whole of $\mathbb{R}$)

$$(\partial_\rho \Phi_0, \partial_\rho(\eta_1-\Phi_1)) - (\Phi_0, \eta_1-\Phi_1) + (\partial_\rho \Phi_1, \partial_\rho(\eta_0-\Phi_0)) \\ + ((\kappa - V)\partial_\rho \Phi_0 - \Phi_1 + W_{,\varphi}(\Phi_0, \mathbf{C}_0, \mathscr{E}(\partial_\rho \mathbf{U}_1 \otimes \nu + \partial_s \mathbf{U}_0 \otimes \tau)), \eta_0 - \Phi_0) \geqslant 0. \quad (5.7)$$

Choosing $\eta_0 = \Phi_0$, we obtain

$$0 \leqslant (\partial_\rho \Phi_0, \partial_\rho(\eta_1-\Phi_1)) - (\Phi_0, \eta_1-\Phi_1) = -\int_{\mathbb{R}} (\partial_{\rho\rho}\Phi_0 + \Phi_0)(\eta_1 - \Phi_1)\, d\rho \quad (5.8)$$

for all η_1 such that $\eta_1(\rho) \leqslant 0$ if $\Phi_0(\rho) = 1$ and $\eta_1(\rho) \geqslant 0$ if $\Phi_0(\rho) = -1$. The integrand to the right in (5.8) is zero if $\rho \in (-\frac{\pi}{2}, \frac{\pi}{2})$. Since we require $\Phi_0 + \varepsilon\Phi_1 + \cdots \in [-1,1]$ to all orders we obtain that $\Phi_1(\rho) \leqslant 0$ if $\Phi_0(\rho) = 1$ and $\Phi_1(\rho) \geqslant 0$ if $\Phi_0 = -1$. Together with (5.8), we obtain $\Phi_1(\rho) = 0$ if $|\Phi_0(\rho)| = 1$.

On the interval $(-\frac{\pi}{2}, \frac{\pi}{2})$, where $|\Phi_0| < 1$, we obtain from (5.7) that

$$-\partial_{\rho\rho}\Phi_1 - \Phi_1 + (\kappa - V)\partial_\rho \Phi_0 + W_{,\varphi}(\Phi_0, \mathbf{C}_0, \mathscr{E}(\partial_\rho \mathbf{U}_1 \otimes \nu + \partial_s \mathbf{U}_0 \otimes \tau)) = 0.$$

Multiplying by $\partial_\rho \Phi_0$ integrating and using integration by parts gives

$$\begin{aligned} 0 &= (\kappa - V)\int_{-\infty}^{\infty} (\partial_\rho \Phi_0)^2 + \int_{-\infty}^{\infty} W_{,\varphi}(\Phi_0, \mathbf{C}_0, \mathscr{E}(\partial_\rho \mathbf{U}_1 \otimes \nu + \partial_s \mathbf{U}_0 \otimes \tau))\partial_\rho \Phi_0 \\ &=: I + II. \end{aligned} \quad (5.9)$$

We compute using (5.5), (5.6) and the fact that $\mathbf{C}_0$, $\mathbf{U}_0$, ν, τ and $W_{,\mathscr{E}}\nu$ do not depend on ρ that

$$\begin{aligned} II &= W(1, \mathbf{C}_0, \mathscr{E}(\nabla \mathbf{u}_0(\mathbf{x}+0))) - W(-1, \mathbf{C}_0, \mathscr{E}(\nabla \mathbf{u}_0(\mathbf{x}-0))) \\ &\quad - \int_{-\infty}^{\infty} W_{,\mathscr{E}}(\Phi_0, \mathbf{C}_0, \mathscr{E}(\partial_\rho \mathbf{U}_1 \otimes \nu + \partial_s \mathbf{U}_0 \otimes \tau)) : (\partial_{\rho\rho}\mathbf{U}_1 \otimes \nu) \\ &= [W]_-^+ - \int_{-\infty}^{\infty} \partial_\rho [(W_{,\mathscr{E}}\nu) \cdot \partial_\rho \mathbf{U}_1] \\ &= [W]_-^+ - [(W_{,\mathscr{E}}\nu) \cdot (\nabla \mathbf{u}_0 \nu)]_-^+, \end{aligned}$$

where we again used the matching conditions (5.2) and (5.4). Since $\int_{-\infty}^{\infty} (\partial_\rho \Phi_0)^2 = \frac{\pi}{2}$, we obtain (3.1).

The continuity equation (3.2) follows as in the paper by Cahn *et al.* [6]. The only difference is that we do allow c to be different from zero before and after the moving front that leads to the jump term that is the only difference from the arguments in [6]. The arguments that have been used in [6] to derive (3.2) can also be used to derive (3.4).

Acknowledgements

This work was supported by the RTN Programme Fronts-Singularities, HPRN-CT-2002-00274 and by the Vielberth Foundation.

https://doi.org/10.1017/S095679250700719X Published online by Cambridge University Press

References

[1] Allen, S. M. & Cahn, J. W. (1977) A microscopic theory of domain wall motion and its experimental verification in Fe–Al alloy domain growth kinetics. *J. Physique* **38**, C7-51–C7-54.

[2] Barrett, J. W., Garcke, H. & Nürnberg, R. (in press) On sharp interface limits of Allen-Cahn/Cahn-Hilliard variational inequalities. *Discrete Contin. Dyn. Syst.*

[3] Barrett, J. W, Nürnberg, R. & Styles, V. (2004) Finite element approximation of a phase field model for void electromigration. *SIAM J. Numer. Anal.* **46**, 738–772.

[4] Blesgen, T. & Weikard, U. (2005) Multi-component Allen–Cahn equation for elastically stressed solids. *Electron. J. Differential Equations* **89**, 1–17.

[5] Blowey, J. F. & Elliott, C. M. (1994) A phase field model with a double obstacle potential. In: G. Buttazzo & A. Visintin (editors), *Motion by Mean Curvature and Related Topics*, de Gruyter, New York, pp. 1–22.

[6] Cahn, J. W., Fife, P. & Penrose, O. (1997) A phase-field model for diffusion-induced grain-boundary motion. *Acta Mater.* **45**, 4397–4413.

[7] Chen, L.-Q. (2002) Phase-field models for microstructure evolution. *Annu. Rev. Mater. Res.* **32**, 113–140.

[8] Ciarlet, P. G. (1978) *The Finite Element Method for Elliptic Problems*, North-Holland, Amsterdam.

[9] Deckelnick, K., Elliott, C. M. & Styles, V. (2001) Numerical diffusion induced grain boundary motion. *Interfaces Free Bound.* **3**, 393–414.

[10] Elliott, C. M. (1997) Approximation of curvature dependent interface motion. State of the art in numerical analysis. In: *IMA Conference Proceedings*, Clarendon Press, Oxford, vol. **63**, pp. 407–440.

[11] Elliott, C. M. & Styles, V. (2003) Computations of bi-directional grain boundary dynamics in thin films. *J. Comput. Phys.* **187**, 524–543.

[12] Eshelby, J. D. (1975) The elastic energy-momentum tensor *J. Elasticity* **5**, 321–335.

[13] Fife, P., Cahn, J. W. & Elliott, C. M. (2001) A free boundary model for diffusion-induced grain-boundary motion. *Interfaces Free Bound.* **3**, 291–336.

[14] Fife, P. & Penrose, O. (1995) Interfacial dynamics for thermodynamically consistent phase-field models with nonconserved order parameter. *Electron. J. Differential Eq.* **16**, 1–49.

[15] Fife, P. & Wang, X-P. (2002) Chemically induced grain boundary dynamics, forced motion by curvature, and the appearance of double seams. *Euro. J. Appl. Math.* **13**, 25–52.

[16] Fratzl, P., Penrose, O. & Lebowitz, J. L. (1999) Modeling of phase separation in alloys with coherent elastic misfit. *J. Statist. Phys.* **95**, 1429–1503.

[17] Fried, E. & Gurtin, M. E. (1994) Dynamic solid–solid transitions with phase characterized by an order parameter. *Physica D* **72**, 287–308.

[18] Garcke, H. (2000) *On Mathematical Models for Phase Separation in Elastically Stressed Solids*, habilitation thesis, University Bonn.

[19] Garcke, H. (2003) On Cahn–Hilliard sytems with elasticity. *Proc. Roy. Soc. Edinburgh.* **133**, A 307–331.

[20] Garcke, H. Mechanical effects in the Cahn–Hilliard model: A review on mathematical results, In: Alain Miranville (editor), *Mathematical Methods and Models in Phase Transitions*, Nova Science Publication, New York, pp. 43–77.

[21] Garcke, H. & Stinner, B. (2006) Second order phase field asymptotics for multi-component systems. *Interfaces Free Bound.* **8**, 131–157.

[22] Garcke, H. & Styles, V. (2004) Bi-directional diffusion induced grain boundary motion with triple junctions. *Interfaces Free Bound.* **6**, 271–294.

[23] Garcke, H. & Weikard, U. (2005) Numerical approximation of the Cahn–Larché equation. *Numer. Math.* **100**, 639–662.

https://doi.org/10.1017/S095679250700719X Published online by Cambridge University Press

[24] Handwerker, C. (1988) Diffusion-induced grain boundary migration in thin films. In: D. Gupta & P. S. Ho (editors), *Diffusion Phenomena in Thin Films and Microelectronic Materials*, Noyes Publication., Park Ridge, NJ, pp. 245–322.

[25] Hu, S. C. & Chen, L. Q. (2001) Solute segregation and coherent nucleation and growth near a dislocation – A phase field model integrating defect and phase microstructures. *Acta Mater*. 49463–472.

[26] Kassner, K. & Misbah, C. (1999) A phase-field approach for stress-induced instabilities. *Europhys. Lett*. **46**, 217–223.

[27] Leo, P. H., Lowengrub, J. S. & Jou, H. J. (1998) A diffuse interface model for microstructural evolution in elastically stressed solids. *Acta Metallurgica* **46**, 2113–2130.

[28] Müller, J. & Grant, M. (1999) Model of surface instabilities induced by stress. *Phys. Rev. Lett*. **82**, 1736–1739.

[29] Mullins, W. W. (1956) Two-dimensional motion of idealized grain boundaries *J. Appl. Phys.* **27**, 900–904.

[30] Penrose, O. (2004) On the elastic driving mechanism in diffusion-induced grain boundary motion. *Acta Materialia* **52**, 3901–3910.

[31] Rubinstein, J., Sternberg, P. & Keller J. B. (1989) Fast reaction, slow diffusion and curve shortening. *SIAM J. Appl. Math.* **49**116–133.

[32] Schmidt, A. & Siebert, K. G. (2005) *Design of Adaptive Finite Element Software. The Finite Element Toolbox ALBERTA*, Lecture Notes in Computational Science and Engineering **42**, Springer-Verlag, Berlin, pp. xii+315.

[33] Sutton, A. P. & Balluffi, R. W. (1995) *Interfaces in Crystalline Materials*, Oxford Science Publications.

https://doi.org/10.1017/S095679250700719X Published online by Cambridge University Press